

Identification of Prime Factors for Efficient Photocatalytic Hydrogen Evolution of Covalent Organic Frameworks via Molecular Engineering

Samrat Ghosh^{1*}, Akinobu Nakada², Maximilian A. Springer^{3,4}, Takahiro Kawaguchi¹, Katsuaki Suzuki⁶, Hironori Kaji⁶, Igor Baburin⁵, Agnieszka Kuc^{3,4}, Thomas Heine^{3,4,5}, Ryu Abe^{2*} and Shu Seki^{1*}

¹Department of Molecular Engineering, Graduate School of Engineering, Kyoto University, Nishikyo-ku, Kyoto 615–8510, Japan.

²Department of Energy and Hydrocarbon Chemistry, Graduate School of Engineering, Kyoto University, Nishikyo-ku, Kyoto 615–8510, Japan.

³Wilhelm–Ostwald–Institute for Physical and Theoretical Chemistry, Linnestrasse 2, 04103 Leipzig, Germany.

⁴Helmholtz–Zentrum Dresden–Rossendorf, Institute for Resource Ecology, Department Reactive Transport, Permoserstrasse 15, 04138 Leipzig, Germany.

⁵Faculty for Chemistry and Food Chemistry, Bergstrasse 66c, 01069 Dresden, Germany.

⁶Institute for Chemical Research, Kyoto University, Uji, Kyoto, 611–0011, Japan.

Abstract

Visible light driven hydrogen (H₂) production from water is a promising strategy to convert and store solar energy as chemical energy. Covalent organic frameworks (COFs) are front runners among different classes of organic photocatalyst, owing to their tunable porosity, crystallinity, optical and electronic properties. Photocatalytic activity of COFs depends on numerous factors such as band gap, crystallinity, porosity, exciton migration, charge separation and transport, stability etc. However, it is challenging to fine tune all these factors simultaneously to enhance the photocatalytic activity. Hence, in this report, we have prioritized

the key factors for efficient photocatalytic H₂ production through structure–property–activity relationship combined with microwave spectroscopy and first–principles calculations. Careful molecular engineering allowed us to tune the light absorption (i.e. band gap), crystallinity, porosity, layer stacking and charge carrier generation and transport of a series of isorecticular COFs. We have assessed how these properties and the interplay between them impact photocatalytic activity of studied COFs. From the structure–property–activity relationship, we found that light absorption and charge carrier generation and transport are the prime factors, which influence the photocatalytic H₂ production of COFs in much greater extent than other factors.

Introduction

H₂ is considered as one of the clean fuels, which can be produced using the inexhaustible sun light and copious water bodies by means of a suitable photocatalyst or photoelectrode.^{1–3} The very first report of such system came from Honda and Fujishima, who demonstrated a n–type TiO₂ photoanode for water oxidation (O₂ production) coupled with Pt counter electrode for water reduction (H₂ production).⁴ Since then, researchers have intuitively studied every single element of the periodic table with the aim of developing new semiconductors, as photocatalysts or photoelectrodes with superior activity for water reduction and/or water oxidation.^{3,5} However, till date, only a very few of them have shown promising activity on a small scale and still needs to go a long way to meet the global energy need.^{6–8} Inspired by natural photosynthesis, chemists have started evaluating small molecular and polymeric organic photocatalysts for H₂ and/or O₂ production from water. The synthetic diversity of organic photocatalyst, allows to tune the light harvesting ability or band gaps, also they are easily processable, light weight and environmentally benign.^{9–12} The real potential of organic photocatalysts was realized when Wang, Domen and coworkers demonstrated relatively

efficient H₂ production from water by graphitic carbon nitride (g-C₃N₄) loaded with Pt co-catalyst in the presence of a sacrificial electron donor (SED) in their pioneering work.¹³ Following this, Copper *et. al.* reported conjugated microporous polymers (CMPs), Thomas *et. al.* reported covalent triazine-based frameworks (CTFs) and Lotsch *et. al.* reported covalent organic frameworks (COFs) with improved light harvesting property and porosity to achieve improved photocatalytic H₂ production.^{14–18} Among these materials, recent studies have revealed that COFs exhibit superior photocatalytic H₂ evolution, due to its crystalline and ordered mesoporous structure.^{18,19,20}

COFs are one of the emerging next generation two- (2D) or three-dimensional (3D) polymeric materials, connected through reversible or irreversible covalent linkages.^{21–25} On demand chemical functionalization, tunable pore size, large surface area, high crystallinity and light weight make COFs a promising material for gas storage and separation, catalysis, energy storage, optoelectronics, sensing and drug delivery.^{26–31} In 2014, Lotsch and co-workers demonstrated H₂ evolution from water using hydrazone-based COFs as photocatalyst loaded with Pt co-catalyst in presence of SED.³² Subsequently, a series of 2D COFs were reported by the same group and by few other groups.^{33–40} Among these systems, a few exhibited very high H₂ production, as comparable or higher to that of g-C₃N₄.^{37,39} These findings opened up new avenues for COFs to emerge as an efficient heterogeneous photocatalyst for H₂ production. Based on the available literature reports, we deduced the factors that affect the photocatalytic performance of COFs in different extent. These include light absorption (i.e. band gap), driving force for proton reduction, exciton migration, charge separation, charge carrier generation and transport, water dispersibility, stacking, crystallinity, porosity, morphology, stability of the transient species, linkage stability, proximity of SED and co-catalyst, as well as the interplay between all of these factors.¹⁸ However, it is challenging to harmonize all the above mentioned factors at the same time to maximize the photocatalytic activity. Hence, it is crucial to identify

the key factors, that affect the photocatalytic H₂ evolution of COFs in greater extent than other factors.

With this objective, herein, we have established a structure–property–activity relationship for COFs, to recognize the prime factors for efficient photocatalytic H₂ production. For this purpose, we have designed and developed a series of 2D isorecticular COFs by careful molecular engineering. Donor–acceptor (D–A) conjugation, torsional angles, and reaction conditions were varied to realize the effect of light absorption, electronic band position, exciton migration, charge carrier generation and transport, layer stacking, crystallinity, porosity and morphology over photocatalytic activity. Furthermore, the structure–property–activity relationship was extrapolated by generating several mixed functional COFs. We have examined the photocatalytic activity of all these COFs under visible light and correlated with the above–mentioned means, what allowed us to identify the prime factors, such as light absorption and charge carrier generation and transport, that would determine the H₂ evolution efficiency in these systems. Through our molecular design, high rate of H₂ evolution ($750\pm25\ \mu\text{mol g}^{-1}\text{ h}^{-1}$) was achieved in the presence of low metallic Pt (1 wt%) co–catalyst and triethanolamine as SED, with long–term stability and reusability.

Results and discussion

Design principle and COF synthesis.

In order to generate β –ketoenamine linked isorecticular COFs, we have chosen 4,4''–diamino substituted *p*–terphenyl (**Tp**) and analogous derivatives as the linker, and condensed with 1,3,5–triformylphloroglucinol (**TH**) (Fig. 1). β –ketoenamine linked COFs are known to have very high chemical stability in water which is desirable for photocatalytic applications and the stability arises from the intramolecular H–bonding.⁴¹ **TpCOF** was previously shown to be a photocatalyst for H₂ evolution, and therefore, we have selected it as our reference to compare

the photocatalytic activity of the newly synthesized COFs.^{38,39} However, it exhibited low photocatalytic activity due to low light absorption and wide band gap of 2.4 eV. To improve the light absorption, band gap, charge separation and transport, the central benzene ring of **Tp** is substituted with electron rich anthracene (**Ant**) and electron deficient benzothiadiazole (**Bt**) or tetrazine (**Tz**) π -conjugated scaffold (Fig. 1). The other intention behind substitution is to tune the torsional angle of the central aryl ring with the peripheral phenyl rings to tune the porosity, crystallinity and stacking of the resulting COFs. **Tp** has a torsional angle of 27°, which is increased to 66° in **Ant** and 39° in **Bt** due to the increase in C–H steric repulsion between the peripheral phenyl rings and the α -proton of anthracene and *N*- of benzothiadiazole, respectively (Fig. 1). Also, C–H steric repulsion diminishes upon replacing the central phenyl with *N*-, resulting in a completely planar **Tz**. These torsional angles were estimated from the single crystal data reported previously.⁴²⁻⁴⁵

All the precursors were synthesized, purified, and characterized using high-resolution mass spectroscopy (HRMS), ¹H and ¹³C nuclear magnetic resonance (NMR). For the construction of β -ketoenamine linked COFs, acid-catalyzed solvothermal condensation was adopted (Fig. 1). **TpCOF150** was synthesized according to the previous reports,³⁹ using condition A (Fig. 1) and a similar condition was used to synthesize the other isorecticular COFs, named as **AntCOF150**, **BtCOF150** and **TzCOF150** (Supplementary Fig. S1). Unfortunately, **AntCOF150** exhibited very low crystallinity, probably due to the large torsional angle of **Ant** and high reaction temperature do not allow proper crystallization of 2D layers.⁴⁷ The reaction conditions were further optimized to obtain crystalline **AntCOF** in good yield employing condition B (Fig. 1). Similarly, other COFs were synthesized using the same condition to improve the crystallinity and named as **AntCOF120**, **BtCOF120**, **TPCOF120** and **TzCOF120** (Supplementary Information). To our surprise, both procedures resulted in COFs with different powder X-ray diffraction pattern although the chemical structure is retained in either case.

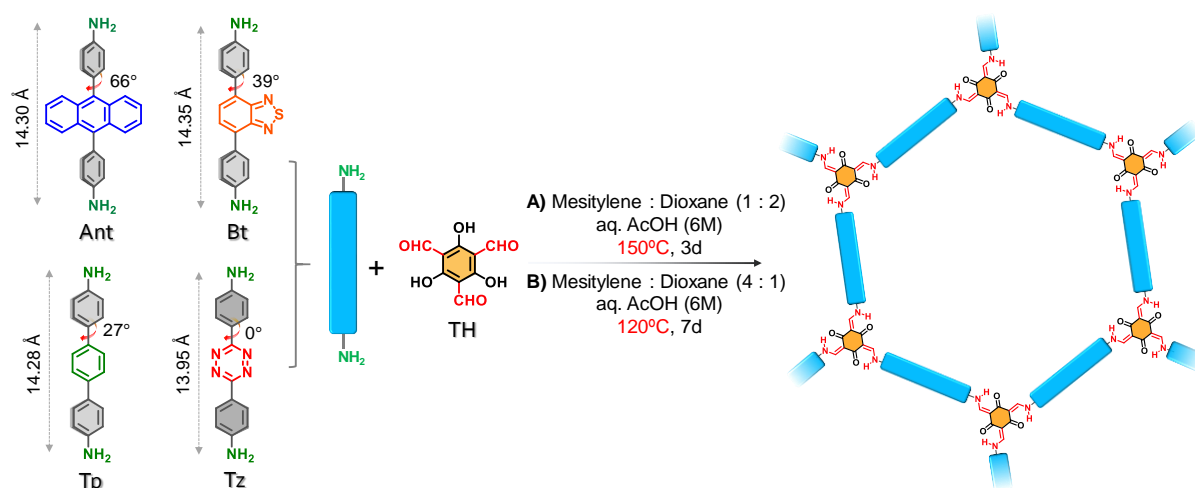


Figure 1| Design and synthesis of the isorecticular COFs for photocatalysis. Structure of the building blocks along with corresponding molecular lengths and torsional angles. Reaction scheme for the synthesis of COFs with different solvothermal conditions, condition A and condition B.

Characterization, crystallinity and structural determination.

Fourier transform infrared (FT-IR) spectra were recorded for all the COFs and compared with their corresponding building blocks (Supplementary Fig. S2). The disappearance of -CHO and -NH_2 stretching frequencies and appearance of peaks at $\sim 1623\text{ cm}^{-1}$ and $\sim 1257\text{ cm}^{-1}$ confirmed the quantitative polymerization through imine bonds.⁴¹ These COFs undergo keto-enol tautomerism and the equilibrium strongly depends on the reaction conditions such as solvent polarity, temperature, and amount of acid catalyst.⁴¹ Hence, we expect the COFs synthesized using condition A and condition B to have different enol- and keto- content, however difficult to assign from the FT-IR because of broad and merged stretching bands. To probe the presence of enol- and keto- form as well as local chemical connectivity, solid state ^{13}C cross polarization magic angle spinning (CP-MAS) NMR spectroscopy was carried out for all the COFs (Supplementary Fig. S3). From all carbon and quaternary carbon spectra, we have obtained -CH carbon spectrum to have better resolution. The assignment of carbons was confirmed by comparing with simulated ^{13}C NMR spectra of model compound using density functional

theory (DFT, B3LYP/6–31G(d)). The absence of –CH carbon peak at around 180–200 ppm confirms the consumption of free –CHO of starting material. Typically, the keto– form exhibits characteristic peak for carbonyl carbon and enamine carbon at ~180–188 and ~109 ppm, respectively, and both peaks were found to shift upfield in the enol form.⁴⁸ We then compared the ¹³C CP–MAS NMR of the identical COFs synthesized under different conditions. COFs prepared at 150 °C showed sharp peak at ~109 ppm, whereas emergence of a new peak at ~102 ppm was observed along with the peak at ~109 ppm for the COFs prepared at 120 °C (Supplementary Fig. S3). This observation clearly indicates that the former COF is mostly composed of keto– form, while later contains both keto– and enol– forms in varied proportions. This would mean that COFs synthesized at 150 °C will have superior chemical stability due to intramolecular hydrogen bonding than COFs synthesized at 120 °C, which is desired for photocatalytic H₂ evolution.^{38,39,41}

In order to understand the effect of molecular torsional angle as well as the keto–enol tautomerism over molecular packing, powder X–ray diffraction (PXRD) analyses were performed for all the COFs (Fig. 2). **BtCOF150**, **TpCOF150** and **TzCOF150** exhibited very similar PXRD pattern with an intense peak at ~2.5° along with few minor peaks, whereas a broad peak was observed for **AntCOF150** at around 3°. For **TzCOF150**, the sharp reflection planes were observed at 2.87°, 4.96°, 5.81°, 7.67° and 10.28°, attributed to the (100), (110), (200), (210) and (220) planes, respectively (Fig. 2d). The last broad peak at ~27.1° in the PXRD patterns can be assigned to (001) plane resulting from the π –stacking of the 2D layers. The maximum intensity of the first peak was observed for **TzCOF150** followed by **TpCOF150** and **BtCOF150**. These results confirm the increase in crystallinity with long range ordering upon decreasing the torsional angle of the linker. Surprisingly, by employing a slight change in reaction conditions, we were successful in getting crystalline COFs using **Ant** linker (**AntCOF120**), although it has large torsional angle (~66°). **AntCOF120** showed different

PXRD pattern compared to COFs synthesized at 150 °C with sharp diffraction peaks at 5.09°, 6.55°, 10.15°, 12.41° and 18.44° corresponding to (110), (200), (220), (130) and (20 $\bar{1}$) planes, respectively (Fig. 2a). We also observed few peaks at higher 2θ arising probably from the interlayer interactions, which are however, difficult to assign. Similar diffraction pattern was observed for **BtCOF120** at 2.82°, 4.64°, 5.75°, 7.28°, 9.33° and 13.68° assignable to (100), (110), (200), (120), (220) and (130) planes, respectively. On the other hand, the diffractogram for **TpCOF120** and **TzCOF120** resemble that of **TpCOF150** and **TzCOF150** (Fig. 2c–d), along with several diffraction peaks at higher 2θ .⁴⁷ To elucidate the stacking of these COFs, three distinct stackings of 2D layers were considered, namely, AA', AB, and ABC (see Fig. 2). Optimized structures were obtained using self-consistent charge density functional based tight-binding (SCC–DFTB) method and Universal Force Field (UFF) classical simulations (see Supplementary Information for details).^{41,46} Similar torsional angles were observed for the optimized COF structures as that of linkers. Due to the high torsional angle of **Ant**, only AB and ABC stackings can be realized because of the steric hindrance. As a result, **AntCOF120** in the ABC stacking is the energetically more favorable phase and the simulated PXRD pattern matches well with the experimental result (Fig. 2a). Also, the experimental PXRD patterns of **BtCOF150**, **TpCOF150** and **TzCOF150** are in a good agreement with the AA' stacking model, which corresponds to AA slipped stacking, where the layers are shifted with respect to each other by small offset (Fig. 2b–d).⁴⁶ On the other hand, the peak positions and relative intensities of **BtCOF120**, **TpCOF120** and **TzCOF120** fit well with the AB stacking model (Supplementary Fig. S4). However, the low resolution of the PXRD does not allow us to distinguish various slipped conformations of AA' stacked structures. Finally, unit cell parameters were estimated by Pawley refinement of experimental PXRD with low residual value. The obtained unit cell parameters match well with the simulated cell parameters obtained from SCC–DFTB (Supplementary Fig. S5).

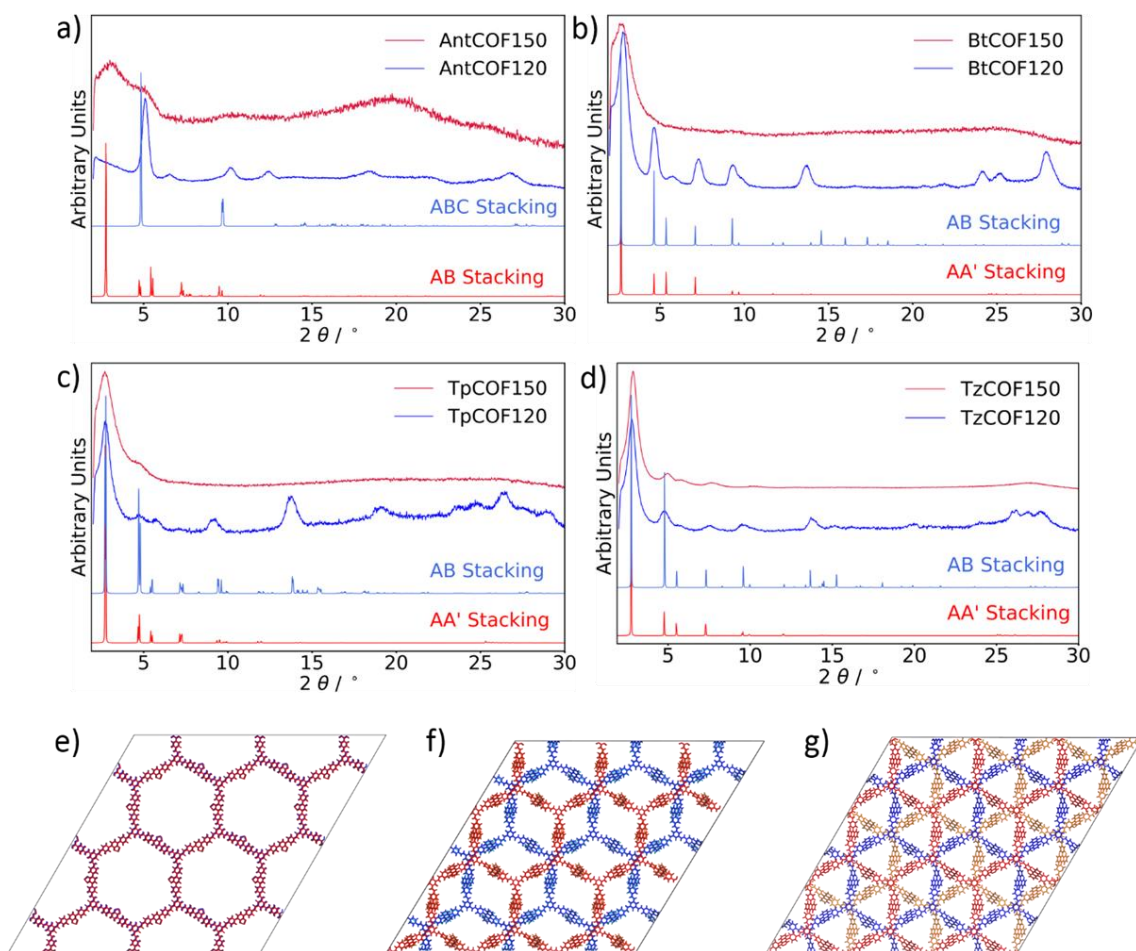


Figure 2| Crystallinity and stacking analysis. Experimental PXRD patterns of a) **AntCOF120** (blue) and **AntCOF150** (red), b) **BtCOF120** (blue) and **BtCOF150** (red), c) **TpCOF120** (blue) and **TpCOF150** (red) and d) **TzCOF120** (blue) and **TzCOF150** (red) compared with the simulated diffraction of each COF. Below, exemplary supercell representations of (e) AA' (**BtCOF**), (f) AB (**AntCOF**), and (g) ABC (**AntCOF**) stackings are shown.

Porosity, morphology and stability.

The permanent porosities of all these COFs were evaluated by nitrogen adsorption–desorption analysis at 77 K. Most of these COFs exhibited type–I isotherm as evident from the adsorption curves, which is a characteristic of microporous materials (Fig. 3). Only **TzCOF150** displayed type–IV isotherm, indicating mesoporous framework (Fig. 3d). The Brunauer–Emmett–Teller (BET) surface areas of COFs synthesized at 150 °C were found to always be higher than those

synthesized at 120 °C, due to the preferred AA' stacking as evident from PXRD (Fig. 3e). The BET surface areas of the four COFs were determined as 660 m² g⁻¹ (**AntCOF150**), 554 m² g⁻¹ (**BtCOF150**), 665 m² g⁻¹ (**TpCOF150**) and 1491 m² g⁻¹ (**TzCOF150**).

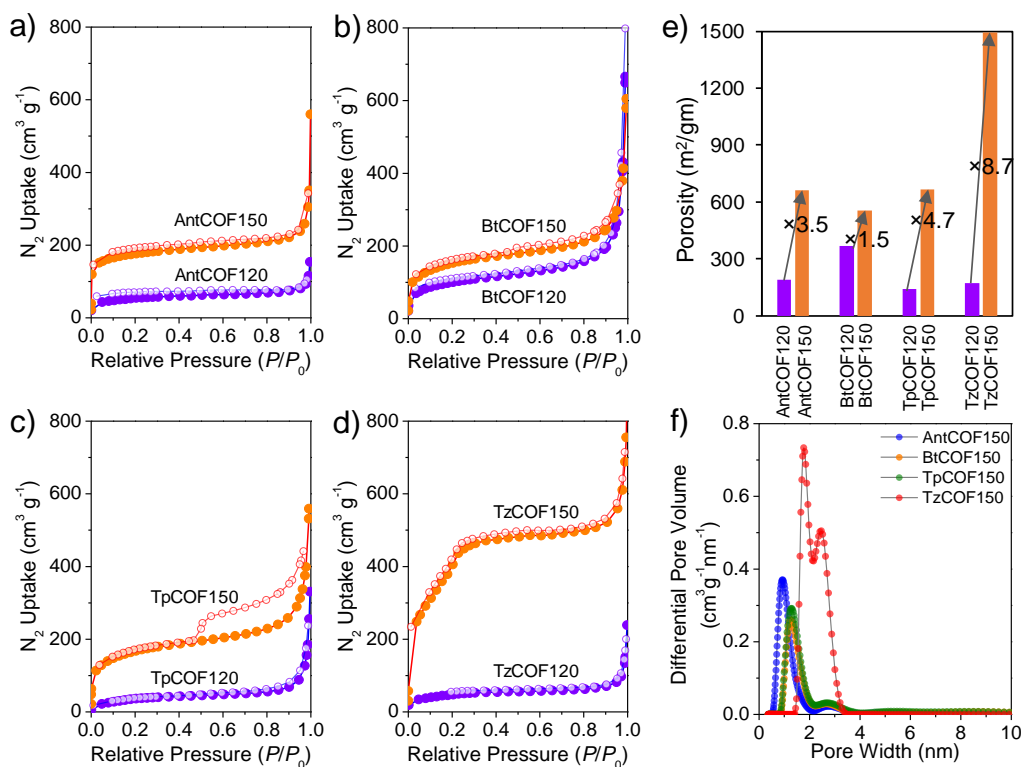


Figure 3| Porosity. Nitrogen sorption isotherms at 77 K for a) **AntCOF120** and **AntCOF150**, b) **BtCOF120** and **BtCOF150**, c) **TpCOF120** and **TpCOF150** and d) **TzCOF120** and **TzCOF150**. Adsorption and desorption denoted by filled and open circles respectively. Comparison of e) the BET surface area and f) the pore-size distribution profiles for the different COFs.

As expected, a gradual increase in the BET surface area was observed upon decreasing the torsional angles of the linkers and **TzCOF150** showed maximum surface area because of the planar structure of the **Tz** (Fig. 3e). However, **AntCOF150** showed slightly higher surface area than **BtCOF150** and **TpCOF150**, probably due to its amorphous microporous polymeric nature. Nonlocal density functional theory (NLDFT) revealed that the pore size distribution of COFs synthesized at 120 °C is smaller than COFs prepared at 150 °C (Fig. 3f, Supplementary

Fig. S6). These results corroborate with the PXRD results and the simulated packing structures. Hence, we have generated two sets of COFs from the same linker, having different crystallinity, stacking arrangement and porosity, to realize the structure–property relationship over photocatalytic H₂ evolution.

Morphology of these COFs were imaged using scanning electron microscopy (SEM) (Supplementary Fig. S7). SEM images revealed that the higher temperature (150 °C) results smaller mesostructured COFs than the lower temperature (120 °C) one, that may help to disperse them better in water, leading to increase in catalytic sites. Thermal stability of all the COFs were analyzed using thermogravimetric analysis (TGA) under nitrogen atmosphere and these COFs exhibited excellent thermal stability up to 400 °C except **TzCOF**, which start to decompose at 250 °C (Supplementary Fig. S8).

Optical and photocatalytic properties.

Prior to the photocatalysis, the light harvesting properties and band gaps of these COFs were assessed using UV–Vis diffuse reflectance spectra (Fig. 4a). The COFs prepared from the same linker showed very similar absorption spectra, in spite of differences in their synthetic condition. **AntCOF150** and **TpCOF150** exhibited narrow optical absorbance with the edge at 500 nm with a wide direct optical bandgap of 2.4 eV (Fig. 4d). Compared to them, **BtCOF150** and **TzCOF150** showed more than 100 nm red shift in absorption onset with a direct optical bandgap of 2.0 eV. Such red shifted broad absorption with lower optical band gap arises from the conjugated D–A structures where benzothiadiazole or tetrazine act as electron acceptors as well as aggregation in the solid state. The highest occupied molecular orbitals (HOMOs) of all the COFs were estimated using photo yield spectroscopy (PYS) (Supplementary Fig. S9) and lowest unoccupied molecular orbitals (LUMOs) were calculated from the optical band gaps and the HOMO energy levels (Fig. 4b). To gain more insights, the frontier molecular orbitals

and energy levels were calculated for the smallest repeating unit of **AntCOF**, **BtCOF**, **TpCOF** and **TzCOF**. Structural optimizations and HOMO–LUMO energy levels were calculated using DFT (B3LYP–/6–31G*). Energy minimized structures revealed that all the torsional angles of linkers remains unchanged in the model COFs. A gradual lowering in LUMO energy levels was observed with the increase in acceptor strengths (Fig. S10), and in line with the experimentally obtained positive shift in the LUMO potential (Fig. 4b). The estimated band gaps are 3.26, 2.74, 3.32 and 2.91 eV for **AntCOF**, **BtCOF**, **TpCOF** and **TzCOF** respectively, which are smaller than the experimental band gaps because we have considered the smallest unit without stacking (Supplementary Fig. S10). However, the DFT calculated energy levels and band gaps well match the experimentally observed trends.

All the synthesized COFs have sufficient driving force for proton reduction except **TzCOF** and the driving force drastically decreases with an increase in the acceptor strength (Fig. 4b). The significant positive potential shift of LUMO in **TzCOF** originates from the low-lying π^* orbital of tetrazine.⁴⁹ Hence, in principle, all the newly synthesized COFs have the ability to do photocatalytic H₂ evolution except **TzCOF**. Next, photocatalytic H₂ production activity of all these COFs were examined under visible light (≥ 400 nm) in the presence of Pt co-catalyst for reducing the overpotential of proton reduction and triethanolamine (TEOA) as SED to regenerate the photocatalyst by capturing the photogenerated holes. In order to compare the photocatalytic activity of all the COFs, same optimized condition was used. As expected, a steady H₂ evolution was detected under visible light illumination (≥ 400 nm) for all the COFs except **TzCOF** in the test period of 24 h (Fig. 4c). Despite having a broad light absorption, highest surface area and crystallinity, **TzCOF** showed no evolution of H₂ due to insufficient driving force for proton reduction (Fig. 4b). Interestingly, **BtCOF150** exhibited very high photocatalytic H₂ evolution rate among the other COFs with a marginal driving force for proton reduction. In general, better photocatalytic activity was observed for COFs synthesized at

150 °C rather than at 120 °C. Average rates of H₂ evolution were calculated at the end of 24 h photocatalysis and found to be 55±5 μmol h⁻¹ g⁻¹, 50±4 μmol h⁻¹ g⁻¹ and 750±25 μmol h⁻¹ g⁻¹ for **AntCOF150**, **TpCOF150** and **BtCOF150**, respectively (Fig. 4c). On the other hand, poor H₂ production was observed for **AntCOF120**, **TpCOF120** and **BtCOF120** with a rate of 16±2 μmol h⁻¹ g⁻¹, 16±2 μmol h⁻¹ g⁻¹ and 95±7 μmol h⁻¹ g⁻¹, respectively. None of the COFs produced H₂ in the absence of Pt catalyst. The photocatalytic activity of **BtCOF150** in presence of low amount of Pt (1 wt%) is comparable with the benchmark systems such as Pt–modified amorphous melon (720 μmol h⁻¹ g⁻¹)⁴⁹ or ‘g–C₃N₄’ (840 μmol h⁻¹ g⁻¹)⁵¹ or crystalline poly(triazineimide) (864 μmol h⁻¹ g⁻¹).⁴⁹ **BtCOF150** showed 15.1 fold higher rate of H₂ evolution compared to **TpCOF150**, whereas with respect to the same **TpCOF**, the previously reported TPBDDACOF and FSCOF exhibited 13.2 times and 6.4 times H₂ evolution rate, respectively (Supplementary Fig. S11).^{38,39} The amount of Pt was varied to improve the photocatalytic activity of **BtCOF150** and found saturation in the photocatalytic activity with 1 wt % Pt (Supplementary Fig. S12a). Also, the apparent quantum yield (AQY) was estimated for **BtCOF150**, and we found 0.2 % AQY at 420 nm. Long term photocatalytic activity of **BtCOF150** was examined and no significant deactivation was observed at least for 120 h, indicating excellent durability and recyclability (Supplementary Fig. S13). Similarly, we have investigated the stability of other COFs using FT–IR and PXRD after 24 h of photocatalysis. FT–IR revealed the retention of molecular connectivity for all the COFs (Supplementary Fig. S14). However, a partial loss in the long range ordering was observed for most of the COFs in different extent as evident from PXRD measurements (Supplementary Fig. S15). This slight loss in crystallinity can be attributed to the delamination of COF layers due to long term photocatalysis in water. Also, photocatalysis does not lead to any major morphological transformation in any of the developed COFs, as evident from the SEM images (Supplementary Fig. S16).

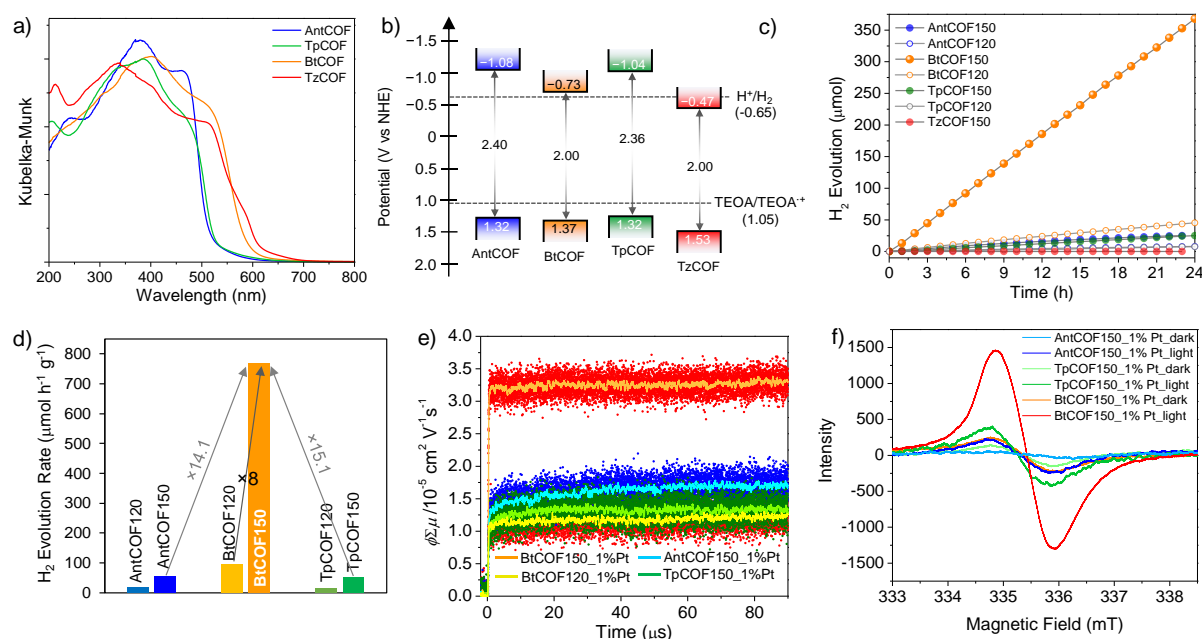


Figure 4| Optical, electronic and photocatalytic properties of isorecticular COFs. a) UV–Vis diffuse reflectance spectra of **AntCOF150**, **BtCOF150**, **TpCOF150** and **TzCOF150** in the solid state. b) HOMO–LUMO energy levels and bandgaps of COFs vs normal hydrogen electrode (NHE), along with the potential of H⁺/H₂ and TEOA/TEOA⁺ at pH =11. c) Time course for photocatalytic H₂ production using visible light for **AntCOF120**, **AntCOF150**, **BtCOF120**, **BtCOF150**, **TpCOF120** and **TpCOF150**. d) Comparison of photocatalytic hydrogen evolution rates. e) Transient photoconductivities of **BtCOF150**, **BtCOF120**, **TpCOF150** and **AntCOF150** loaded with 1 wt% Pt. f) EPR spectra of **AntCOF150**, **TpCOF150** and **BtCOF150** loaded with 1 wt% Pt, in presence of light and dark.

In order to prioritize the key factors for efficient H₂ evolution, we have correlated the photocatalytic activity of all the COFs with the torsional angle, porosity, crystallinity, stacking, light absorption, band gap, driving force for proton reduction and photoconductivity in the following section (Table 1). **AntCOF120** possesses higher crystallinity compared to **AntCOF150** but showed ~3.5 times reduced rate of H₂ production. This can be correlated with the ~3.5 times decrease in surface area for **AntCOF120** compared to **AntCOF150**, since both the COFs have same light harvesting ability and band position (Fig. 4c). Similarly, **TpCOF120** and **TpCOF150** both have similar crystallinity, light absorption, band position and the three

times higher rate of H₂ production in the later can be attributed to the increase in surface area (~4.7 times). **BtCOF150** exhibited enhanced photocatalytic activity than **TpCOF150** despite having reduced driving force for the proton reduction, lesser crystallinity and surface area compared to the later (Table 1). Probably the broad light absorption (i.e. low band gap) and better charge carrier generation and transport of D–A conjugated **BtCOF150** plays an important role compared with the other factors (Table 1). To estimate the effect of light absorption, wavelength dependent H₂ evolution measurements were performed for all the COFs using different band-pass filters and compared with the UV–Vis spectra. Both **BtCOF120** and **BtCOF150** showed H₂ evolution activity up to 600 nm, while negligible H₂ evolution was observed for the other COFs beyond 550 nm (Supplementary Fig. S12b and S12c). To our surprise, **BtCOF150** showed eight fold increased rate of H₂ evolution compared to **BtCOF120**, although both have comparable crystallinity, similar light absorption, bandgaps and the driving force for proton reduction. Hence, it is clear that such an increase in the photocatalytic activity arises from the cumulative effect of increase in surface area, stacking and charge carrier mobility. However, the surface area increase was only 1.5 times (Fig. 3e), which clearly state that stacking and charge transport has a major say in the increase in photocatalytic activity.

Table 1| Torsional angles, surface area, crystallinity, photophysical properties and the rate of H₂ evolution of all the COFs.

COF	Torsional angle (°)	BET surface area (m ² g ⁻¹)	Degree of Crystallinity	Stacking ^a	Normalized light absorption area (nm ²) ^b	Bandgap (eV) ^c	Driving force (V) ^d	Rate of H ₂ evolution (μmol g ⁻¹ h ⁻¹) ^e	Photoconductivity ($\phi\Sigma\mu$, 10 ⁻⁵ cm ² V ⁻¹ s ⁻¹) ^f
AntCOF120	66	191	Crystalline	ABC	91.8	2.40	-0.43	16±2	0.5
AntCOF150	66	660	Amorphous	AB	91.8	2.40	-0.43	55±5	1.2
BtCOF120	39	368	Crystalline	AB	134.8	2.00	-0.08	95±7	1.0
BtCOF150	39	554	Semicrystalline	AA'	134.8	2.00	-0.08	750±25	3.2
TpCOF120	27	141	Semicrystalline	AB	89.7	2.36	-0.39	16±2	0.6
TpCOF150	27	665	Semicrystalline	AA'	89.7	2.36	-0.39	50±4	1.1
TzCOF150	0	1491	Crystalline	AA'	142.7	2.00	0.18	0	0.2

^aCalculated from theoretical simulation. ^bBetween 400–800 nm. ^cEstimated from absorption onset. ^dDriving force for proton reduction = (LUMO – 0.65 (potential of H⁺/H₂)) V vs NHE at pH=11. ^eAll rates were measured using the same instruments, optical setup and reaction conditions. ^fEvaluated using FP–TRMC measurement under identical condition.

Microwave spectroscopy and band structures.

To support the above mentioned notion, the photoconductivity of all the COFs were measured using flash–photolysis time–resolved microwave conductivity (FP–TRMC). FP–TRMC is a powerful electrodeless method to access the intrinsic/local charge transporting property of semiconductors, that provides a measure of photoconductivity as $\phi\Sigma\mu$, where ϕ and $\Sigma\mu$ corresponds to the charge carrier generation quantum yield and the total charge carrier mobilities (electron + hole mobilities), respectively.^{52–55} For FP–TRMC measurements, COF pellets were placed over quartz substrate and excited with 355 nm laser excitation. Negligible photoconductivity was observed for all the pristine COFs upon light excitation, probably due to a very small charge separation between the COF layers. A significant enhancement in photoconductivity was observed for the COFs loaded with 1 wt% Pt nanoparticle because of the photogenerated charge separation and transport (Fig. 4e). Maximum photoconductivity of

$3.2 \times 10^{-5} \text{ cm}^2 \text{ V}^{-1}\text{s}^{-1}$ was observed for the **BtCOF150_1%Pt**, which is 3 times higher than the **BtCOF120_1%Pt**, indicating the improvement in $\Sigma\mu$ rather than ϕ , because both COFs bear the same chromophore. All the kinetic traces of the photoconductivity transients show long lifetimes over 100 μs , suggesting the significant contribution from the free charge carriers of holes on COFs and electrons on Pt co-catalysts. Note that the Pt co-catalysts exist as nanoparticles and confining electrons within the particles, contributing very small to the photoconductivity transients. The yield of the charge carriers (ϕ) could be roughly estimated from the AQY of H_2 production, assuming quantitative conversion of charge carries for proton reduction. Hence, the estimated ϕ for **BtCOF150** is 2×10^{-3} and the deduced hole mobility is $0.016 \text{ cm}^2 \text{ V}^{-1}\text{s}^{-1}$. Unfortunately, low intensity of the monochromatic light does not allow us to estimate the AQY of other COFs. If we consider the same value of ϕ for **BtCOF120**, the estimated hole mobility is $0.005 \text{ cm}^2 \text{ V}^{-1}\text{s}^{-1}$, which is 3 times lower than **BtCOF150**.

To have a theoretical support, band structures were calculated for the AA', and AB stacked **BtCOF**, within $k_B T$ at room temperature, both are direct-gap semiconductors with calculated bandgap of 1.3 eV. These band gaps are smaller than the experimentally measured ones, which is as expected, because DFTB tends to underestimate them. Interestingly, AA' stacked structure exhibits strong dispersion in the conduction band edge compared to the AB stacked **BtCOF** (Supplementary Fig. S17). As a result, the effective masses electrons are smaller for the AA' stacking, possibly leading to higher charge carrier mobility (Supplementary Table S2).⁵⁶ These results clearly corroborate with trends in charge carrier mobilities obtained from the FP-TRMC measurement. On the other hand, **AntCOF120** and **TpCOF150** exhibited similar photoconductivity as **BtCOF120**, although slightly better photocatalytic activity was obtained for **BtCOF120** because of higher light absorption area compared to the **AntCOF120** and **TpCOF150** (Table 1). The photoconductivity results are in line with the observed H_2 production activity of the COFs. These results confirm that the local charge carrier mobility is

one of the prime factors that affect the photocatalytic H_2 evolution in greater extent. Moreover, light induced charge carrier generation was revealed using another microwave based technique, electron paramagnetic resonance (EPR) spectroscopy. **BtCOF150_1%Pt** exhibited a signal at $g = 2.004$ which intensified upon visible light excitation, indicating charge carrier generation (Fig. 4f). Compared to **BtCOF150_1%Pt**, all other COFs showed very low intensity, due to the reduced generation of charge carriers. Also, we have performed the same experiment for the pristine COFs (without Pt) and again **BtCOF150** showed intense signal compared to **AntCOF150** and **TpCOF150** (Supplementary Fig. S18). It is noteworthy to mention that in general Pt loaded COFs showed higher signal intensities compared with the pristine COFs upon light illumination, indicating charge separation between COFs and Pt co-catalyst. These results are in line with the photoconductivity data obtained from the FP-TRMC measurement.

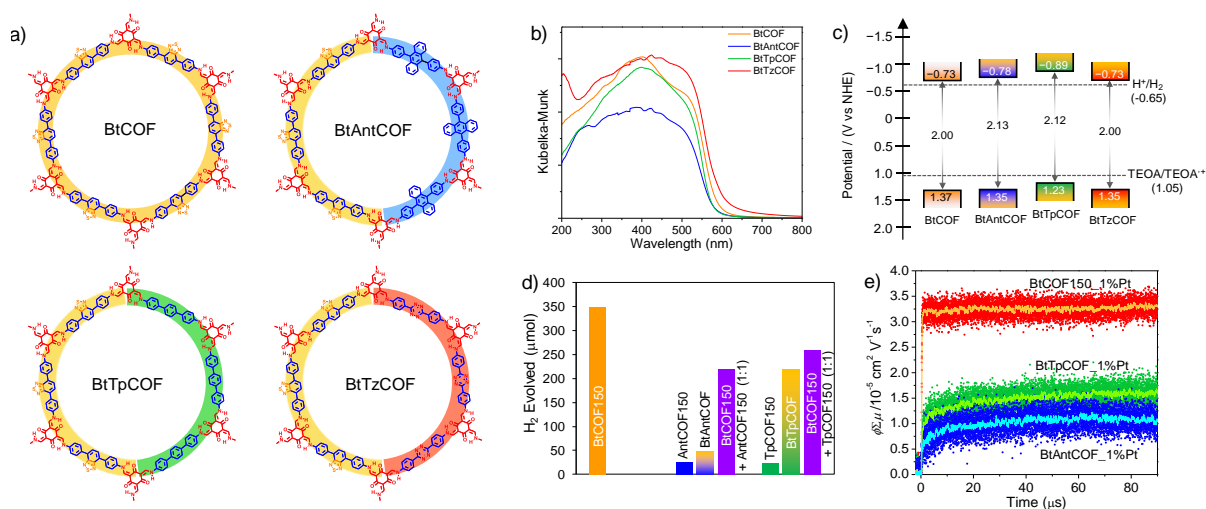


Figure 5| Photocatalytic and optoelectronic performance of mixed functional COFs. a) Chemical structures of mixed COFs. b) UV-Vis diffuse reflectance spectra of the mixed COFs in the solid state. c) HOMO-LUMO energy levels and bandgaps of COFs vs NHE, along with the potential of H^+/H_2 and $\text{TEOA}/\text{TEOA}^{+}$ at pH = 11. d) Comparison of photocatalytic H_2 production of mixed COFs with the parent COFs under visible light irradiation after 24 h. e) Transient photoconductivities of **BtCOF150**, **BtAntCOF** and **BtTpCOF** loaded with 1 wt% Pt.

Optical and photocatalytic properties of mixed COFs.

Finally, we have done the bandgap engineering of the COFs to enhance the light harvesting property and charge separation and understand their effects on the photocatalytic H₂ evolution. Our unique molecular design has allowed us to create mixed or doped COFs due to very similar linkers geometry and length (Fig. 1). Moreover, we have the freedom to modulate the porosity and crystallinity using this approach. This can further lead us to establish a structure–property–activity relationship, which can validate our hypothesis. For this, we have incorporated **Bt** linker in the frameworks of **AntCOF**, **TpCOF** and **TzCOF** to boost their photocatalytic activity (Fig. 5a). **BtAntCOF**, **BtTpCOF** and **BtTzCOF** was synthesized by taking the corresponding linkers (1:1) and condensed with **TH** in equimolar ratio using condition A (Supplementary Information). Formation of mixed COFs were confirmed using FT–IR, ¹³C CP–MAS NMR and PXRD (Supplementary Fig. S19, Fig. S20 and Fig. S21). ¹³C CP–MAS NMR revealed that the mixed COFs are mostly composed of keto– form, due to the absence of peak at ~102 ppm correspond to the –enol form. **BtAntCOF** showed better crystallinity compared to **AntCOF150** due to the introduction of low torsional angle **Bt** linker which rigidifies the framework (Supplementary Fig. S21a). Similarly, insertion of **Tp** and **Tz** linkers with lower torsional angle than **Bt**, enhances the crystallinity of **BtTpCOF** and **BtTzCOF** significantly, compared with **BtCOF150** (Supplementary Fig. S21b and S21c). **BtAntCOF** and **BtTpCOF** showed better surface area than the parent COFs, whereas decrease in surface area was observed for **BtTzCOF** (Supplementary Fig. S22). Color change as well as red shifted broad absorption of all the mixed COFs confirmed uniform mixing of the linkers (Fig. 5b, Supplementary Fig. S1). Also, mixing leads to a significant decrease in the direct optical band gap from 2.4 eV to 2.1 eV for both **BtAntCOF** and **BtTpCOF**, whereas for **BtTzCOF**, the band gap remains unchanged compared to parent COFs (Fig. 5c). Notably, mixing with **Bt** linker decreases the LUMO level of **TzCOF** and **BtTzCOF** has marginal driving force to carry

out the proton reduction. Next, we have checked the photocatalytic H₂ production activity of all the mixed COFs under the same conditions as used for the parent COFs (Supplementary Fig. S23). Figure 5d shows a comparative plot of the amount of H₂ produced during a test period of 24 h. **BtTpCOF** produced maximum H₂ among other mixed COFs, whereas **BtAntCOF** showed slight improvement compared to **AntCOF150** and still no H₂ evolution was observed for **BtTzCOF**. Mixing leads to ~9 times improvement in photocatalytic activity for **BtTpCOF** compared to **TpCOF150**, although crystallinity decreases with a ~1.8 times increase in surface area, confirming the key role of light harvesting property as well as band position to improve photocatalytic activity. However, despite having higher surface area, moderate crystallinity and similar light absorption, ~7 and ~1.6 times lower photocatalytic activity was observed for **BtAntCOF** and **BtTpCOF** compared to **BtCOF150** (Supplementary Table S2). In order to have a comparison, we have physically mixed equal amounts (1:1 wt ratio) of **AntCOF150** with **BtCOF150** and **TpCOF150** with **BtCOF150** and both the physical mixture exhibited superior H₂ production compared to chemically mixed **BtAntCOF** and **BtTpCOF**, with ~1.6 and ~1.3 times lower photocatalytic activity compared to **BtCOF150**. Theoretically, one can expect 2 times or lower photocatalytic H₂ production for both chemically and physically mixed COFs than **BtCOF150** because of 2 times reduction in the amount of **BtCOF150**. These results point to the random arrangement of linkers inside the chemically mixed COFs, which drastically decreases the charge carrier mobility. However, better photocatalytic **BtTpCOF** suggests the possibility of self-sorted domains of **BtCOF** and **TpCOF** in **BtTpCOF**, which is difficult to confirm. To precisely probe the charge carrier generation and transport, we have checked the photoconductivity of mixed COFs by FP-TRMC and compared with **BtCOF150** (Fig. 5e). Both the mixed COFs showed much lower photoconductivity compared to **BtCOF150**, thus suggesting that the conductive path of **BtCOF150** was blocked by the random arrangement of chromophores. Also, it can be deduced

that high torsional angle of **Ant** causes AB stacking in **BtAntCOF**. On the other hand, lower torsional angle of **Tp** prefers AA' stacking and keep some conductive paths open in **BtTpCOF** resulting moderate H₂ production.

Conclusions

In summary, we have designed and synthesized novel isorecticular 2D COFs via systematic molecular engineering of the building blocks, that leads to a gradual change in porosity, crystallinity, stacking, optical and electronic properties. As a result, these COFs exhibited different photocatalytic H₂ production under visible light and we have successfully correlated their photocatalytic activity with the above-mentioned factors. We have observed an exponential dependence of light absorption and charge transport with photocatalytic H₂ evolution, whereas porosity and crystallinity showed linear dependence for the COFs, in line with the previous reports.^{33,38} Also, it is important to mention that, AA', AB and ABC stacked COFs all are crystalline, but our results indicate that AA' stacking exhibits better photocatalytic activity among others because it dramatically improves the exciton migration and charge transport. As a result, **BtCOF150** showed maximum rate of H₂ evolution ($750 \pm 25 \mu\text{mol g}^{-1} \text{h}^{-1}$) among all the developed COFs, in presence of low metallic Pt (1 wt%) co-catalyst, comparable to g-C₃N₄ and benchmark COFs reported previously.¹⁸ Furthermore, a negative effect on the H₂ evolution was observed upon introducing dissimilar linkers into **BtCOF150**, although there was an increase in porosity and crystallinity. This finding again manifests the immense role of charge carrier mobility over other factors. All the results are well supported by the photoconductivity measurement (FP-TRMC), EPR and DFTB calculations. Although, in the present work we are unable to control or tune the water dispersibility, proximity of SED and co-catalyst, and assume to be similar for all the generated COFs. The structure-property-

activity correlation presented here will pave the way to the design of highly efficient COF photocatalyst with enhanced activity.

Methods

Photocatalytic Hydrogen evolution experiments.

Photocatalytic reactions were carried out in a Pyrex reaction vessel connected to a glass closed gas circulation system. A suspension of photocatalyst (20 mg) in 100 mL water–triethanolamine mixed solution (4:1 v/v) containing appropriate amounts of H_2PtCl_6 was evacuated and purged with Ar (ca. 10 kPa). Visible light was irradiated to the reaction cell using a Xe lamp (Cermax, 300 W) fitted with a CM–1 cold mirror and cut-off filters. Pt co-catalyst was loaded *in-situ* from photoreduction of H_2PtCl_6 . The evolved H_2 was analyzed by a gas chromatography (GC–8A, Shimadzu, TCD detector, MS 5A column, Ar carrier) connected to the closed gas circulation system (Supplementary Fig. S24).

Flash–Photolysis Time Resolved Microwave Conductivity (FP–TRMC).

The charge carrier transport property was evaluated by FP-TRMC technique at room temperature under ambient condition. Transient charge carriers were generated through photoexcitation by laser pulses of third harmonic generation ($\lambda = 355 \text{ nm}$) from a Spectra Physics INDI-HG Nd:YAG laser with a pulse duration of 5–8 ns at the photon density of $4.6 \times 10^{15} \text{ photon cm}^{-2}$. The frequency and power of probing microwave were set at around 9.1 GHz and 3 mW, respectively so that the electric field of the microwave was sufficiently small not to disturb the motion of charge carriers. Photoconductivity transients, demodulated through a GaAs crystal-diode with Schottky-barriers (rise time $< 1 \text{ ns}$), were monitored by a Tektronix model TDS3032B digital oscilloscope. Time constant (τ) of the present TRMC system was

then determined by the Q-value of microwave cavity ($Q = 2000$), leading to $\tau = Q/2f \sim 100$ ns.

The observed conductivities were normalized, given by a photocarrier generation yield (ϕ) multiplied by sum of the carrier mobilities of electron/hole ($\Sigma\mu$), according to the equation,

$$\phi\Sigma\mu = (A\Delta P_r)/(eI_0F_LP_r)$$

where, e , A , I_0 , F_L , P_r , and ΔP_r are elementary charge, sensitivity factor ($S\text{ cm}^{-1}$), incident photon density of the excitation laser (photon cm^{-2}), correction factor (cm^{-1}) for overlapping between special distribution of photo-generated charge carriers and electromagnetic field strength of probing microwave in the cavity, and reflected microwave power and its transient change, respectively. COF pallets were prepared and fixed over quartz substrate using tape for the FP-TRMC measurements.

Acknowledgments

This work was partly supported by a Grant-in-Aid for Scientific Research (no. 26102011, 15K21721, 17H06439, 19F19044 and 18H03918) from the Japan Society for the Promotion of Science (JSPS). M. S., A. K., I. B., and T. H. thank the high-performance computing centre, ZIH Dresden, for computer time and recourses, and Deutsche Forschungsgemeinschaft for financial support (SPP 1928, HE 3543/31-1). It is our pleasure to thank Prof. Koichi Eguchi for allowing T.K. to perform the nitrogen isotherm. Dr. Y. Tsutsui, Dr. T. Sakurai and Dr. W. Masuda are acknowledged for the fruitful discussions.

Authors contribution:

S.G. and S.S. conceived the project idea, designed the experiments and wrote the manuscript. S.G. synthesized the COFs and performed the characterizations. A.N. and R.A. had performed the photocatalysis, PYS and absorption experiments. M.S., A.K., I.B. and T.H. conceived the modelling strategy of periodic structures using AMS and dftb+ software, performed the

structural calculations (UFF and DFTB) and calculated the band structures (DFTB). Gaussian molecular calculations performed by S.G. T.K. carried out nitrogen isotherm. Solid state NMR was carried out by K.S. and H.K. Photoconductivity experiments were carried out by S.G. and S.S. All the authors have interpreted corresponding data and contributed in the preparation of the manuscript.

Competing interests

The authors declare no competing interests.

References

1. Kudo, A. & Miseki, Y. Heterogeneous photocatalyst materials for water splitting. *Chem. Soc. Rev.* **38**, 253–278 (2009).
2. Pinaud, B. A. et al. Technical and economic feasibility of centralized facilities for solar hydrogen production via photocatalysis and photoelectrochemistry. *Energy Environ. Sci.* **6**, 1983–2002 (2013).
3. Wang, Y. et al. Mimicking natural photosynthesis: solar to renewable H₂ fuel synthesis by Z-scheme water splitting systems. *Chem. Rev.* **118**, 5201–5241 (2018).
4. Fujishima, A. & Honda, K. Electrochemical photolysis of water at a semiconductor electrode. *Nature* **238**, 37–38 (1972).
5. Chen, S., Takata, T. & Domen, K. Particulate photocatalysts for overall water splitting. *Nat. Rev. Mater.* **2**, 17050 (2017).
6. Liao, L. et al. Efficient solar water-splitting using a nanocrystalline CoO photocatalyst. *Nat. Nanotechnol.* **9**, 69–73 (2014).
7. Kibria, M. et al. Visible light-driven efficient overall water splitting using p-type metal-nitride nanowire arrays. *Nat. Commun.* **6**, 6797 (2015).

8. Wang, Q. et al. Scalable water splitting on particulate photocatalyst sheets with a solar-to-hydrogen energy conversion efficiency exceeding 1%. *Nat. Mater.* **15**, 611–615 (2016).
9. Yanagida, S., Kabumoto, A., Mizumoto, K., Pac, C. & Yoshino, K. Poly(para) phenylene-catalyzed photoreduction of water to hydrogen. *Chem. Commun.* **8**, 474–475 (1985).
10. Caputo, C. A. et al. Photocatalytic hydrogen production using polymeric carbon nitride with a hydrogenase and a bioinspired synthetic Ni catalyst. *Angew. Chem. Int. Ed.* **53**, 11538–11542 (2014).
11. Liu, J. et al. Metal-free efficient photocatalyst for stable visible water splitting via a two-electron pathway. *Science* **347**, 970–974 (2015).
12. Zhang, G., Lan, Z.-A. & Wang, X. Conjugated polymers: catalysts for photocatalytic hydrogen evolution. *Angew. Chem. Int. Ed.* **55**, 2–18 (2016).
13. Wang, X. et al. A metal-free polymeric photocatalyst for hydrogen production from water under visible light. *Nat. Mater.* **8**, 76–80 (2009).
14. Sprick, R. S. et al. Tunable organic photocatalysts for visible-light-driven hydrogen evolution. *J. Am. Chem. Soc.* **137**, 3265–3270 (2015).
15. Kuhn, P., Antonietti, M. & Thomas, A. Porous, covalent triazine-based frameworks prepared by ionothermal synthesis. *Angew. Chem. Int. Ed.* **47**, 3450–3453 (2008).
16. Jiang, X., Wang, P. & Zhao, J. 2D covalent triazine framework: a new class of organic photocatalyst for water splitting. *Journal of Materials Chemistry A* **3**, 7750–7758 (2015).
17. Kuecken, S. et al. Fast tuning of covalent triazine frameworks for photocatalytic hydrogen evolution. *Chem. Commun.* **53**, 5854–5857 (2017).

18. Banerjee, T. et al. H₂ evolution with covalent organic framework photocatalysts. *ACS Energy Lett.* **3**, 400–409 (2018).
19. Vyas, V. S., Lau, V. W. H. & Lotsch, B. V. Soft photocatalysis: organic polymers for solar fuel production. *Chem. Mater.* **28**, 5191–5204 (2016).
20. Thote, J. et al. A covalent organic framework-cadmium sulfide hybrid as a prototype photocatalyst for visible-light-driven hydrogen production. *Chem. Eur. J.* **20**, 15961–15965 (2014).
21. Feng, X., Ding, X. S. & Jiang, D. Covalent organic frameworks. *Chem. Soc. Rev.* **41**, 6010–6022 (2012).
22. Colson, J. W. & Dichtel, W. R. Rationally synthesized two-dimensional polymers. *Nat. Chem.* **5**, 453 (2013).
23. Diercks, C. S. & Yaghi, O. M. The atom, the molecule, and the covalent organic framework. *Science* **355**, eaal1585 (2017).
24. Lohse, M. S. & Bein, T. Covalent organic frameworks: structures, synthesis, and applications. *Adv. Funct. Mater.* **28**, 1705553 (2018).
25. Kandambeth, S., Dey, K. & Banerjee, R. Covalent organic frameworks: chemistry beyond the structure. *J. Am. Chem. Soc.* **141**, 1807–1822 (2019).
26. Huang, N., Wang, P. & Jiang, D. Covalent organic frameworks: a materials platform for structural and functional designs. *Nat. Rev. Mater.* **1**, 16068 (2016).
27. Mal, A. et al. Supramolecular reassembly of self-exfoliated ionic covalent organic nanosheets for label-free detection of double-stranded DNA. *Angew. Chem. Int. Ed.* **130**, 8443–8447 (2018).
28. Segura, J. L., Mancheño, M. J. & Zamora, F. Covalent organic frameworks based on schiff-base chemistry: synthesis, properties and potential applications. *Chem. Soc. Rev.* **45**, 5635–5671 (2016).

29. Mandal, A. K., Mahmood, J., & Baek, J. B. Two-dimensional covalent organic frameworks for optoelectronics and energy storage. *ChemNanoMat* **3**, 373–391 (2017).
30. Beuerle, F. & Gole, B. Covalent organic frameworks and cage compounds: design and applications of polymeric and discrete organic scaffolds. *Angew. Chem., Int. Ed.* **57**, 4850–4878 (2018).
31. Song, Y., Sun, Q., Aguila, B., and Ma, S. Opportunities of Covalent Organic Frameworks for Advanced Applications. *Adv. Sci.* **6**, 1801410 (2019).
32. Stegbauer, L., Schwinghammer, K. & Lotsch, B. V. A hydrazone-based covalent organic framework for photocatalytic hydrogen production. *Chem. Sci.* **5**, 2789–2793 (2014).
33. Vyas, V. S. et al. A tunable azine covalent organic framework platform for visible light-induced hydrogen generation. *Nat. Commun.* **6**, 8508 (2015).
34. Haase, F. et al. Structure-property-activity relationships in a pyridine containing azine-linked covalent organic framework for photocatalytic hydrogen evolution. *Faraday Discuss.* **162**, 165–169 (2017).
35. Banerjee, T. et al. Single site photocatalytic H₂ evolution from covalent organic frameworks with molecular cobaloxime co-catalysts. *J. Am. Chem. Soc.* **139**, 16228–16234 (2017).
36. Sick, T. et al. Oriented films of conjugated 2D covalent organic frameworks as photocathodes for water splitting. *J. Am. Chem. Soc.* **140**, 2085–2092 (2018).
37. Bi, S. et al. Two-dimensional semiconducting covalent organic frameworks via condensation at arylmethyl carbon atoms. *Nat. Commun.* DOI: 10.1038/s41467-019-10504-6 (2019).
38. Pachfule, P. et al. Diacetylene functionalized covalent organic framework (COF) for photocatalytic hydrogen generation. *J. Am. Chem. Soc.* **140**, 1423–1427 (2018).

39. Wang, X. et al. Sulfone-containing covalent organic frameworks for photocatalytic hydrogen evolution from water. *Nat. Chem.* **10**, 1180–1189 (2018).
40. Jin, E. et al. 2D sp² Carbon-conjugated covalent organic frameworks for photocatalytic hydrogen production from water. DOI: 10.1016/j.chempr.2019.04.015 (2019).
41. Kandambeth, S. et al. Construction of crystalline 2D covalent organic frameworks with remarkable chemical (acid/base) stability via a combined reversible and irreversible route. *J. Am. Chem. Soc.* **134**, 19524–19527 (2012).
42. Rietveld, H. M. & Maslen EN, An X-ray and neutron diffraction refinement of structure of *para*-terphenyl. *Acta Crystallogr* **B26**, 693–706 (1970).
43. Kato, S.-I. et al. Novel 2,1,3-benzothiadiazole-based red-fluorescent dyes with enhanced two-photon absorption cross sections. *Chem.–Eur. J.* **12**, 2303–2317 (2006).
44. Langer, V. & Becker, H.-D. Crystal structure of 9,10-diphenylanthracene, (C₆H₅)(C₁₄H₈)(C₆H₅). *Z. Kristallogr.*, **199**, 313–315 (1992).
45. Ahmed, N. A., & Kitaigorodsky, A. I. Experimental and theoretical determination of the crystal structure of 3,6-diphenyl-s-tetrazine. *Acta Crystallogr.* **B28**, 739–742 (1972).
46. Lukose, B., Kuc, A. & Heine, T. The structure of layered covalent-organic frameworks. *Chem. Eur. J.* **17**, 2388–2392 (2010).
47. Thompson, C. M. et al. Computational and experimental studies on the effects of monomer planarity on covalent organic framework formation. *J. Am. Chem. Soc.* **139**, 10506–10513 (2017).
48. Albacete, P. et al. Layer-stacking-driven fluorescence in a two-dimensional imine-linked covalent organic framework. *J. Am. Chem. Soc.* **140**, 12922 (2018).
49. Yuasa, J., Mitsui, A. & Kawai, T. π – π^* Emission from a tetrazine derivative complexed with zinc ion in aqueous solution: a unique water-soluble fluorophore. *Chem. Commun.* **47**, 5807–5809 (2011).

50. Schwinghammer, K. et al. Triazine-based carbon nitrides for visible-light driven hydrogen evolution. *Angew. Chem. Int. Ed.* **52**, 2435–2439 (2013).
51. Zhang, J. et al. Synthesis of a carbon nitride structure for visible-light catalysis by copolymerization. *Angew. Chem. Int. Ed.* **49**, 441–444 (2010).
52. Seki, S., Saeki, A., Sakurai, T. & Sakamaki, D. Charge carrier mobility in organic molecular materials probed by electromagnetic waves. *Phys. Chem. Chem. Phys.* **16**, 11093–11113 (2014).
53. Saeki, A., Koizumi, Y., Aida, T. & Seki, S. Comprehensive approach to intrinsic charge carrier mobility in conjugated organic molecules, macromolecules, and supramolecular architectures. *Acc. Chem. Res.* **45**, 1193–1202 (2012).
54. Ding, X. et al. Synthesis of metallophthalocyanine covalent organic frameworks that exhibit high carrier mobility and photoconductivity. *Angew. Chem. Int. Ed.* **50**, 1289–1293 (2011).
55. Wan, S. et al. Covalent organic frameworks with high charge carrier mobility. *Chem. Mater.* **23**, 4094–4097 (2011).
56. Jing, Y.; Heine, T. Two-dimensional kagome lattices made of hetero triangulenes are Dirac semimetals or single-band semiconductors. *J. Am. Chem. Soc.* **141**, 743–747 (2019).

Supplementary Information

Index

Sl.No.		Page No:
1.	Materials and methods	3
	1.1 Solution state nuclear magnetic resonance	3
	1.2 Solid state nuclear magnetic resonance	3
	1.3 High resolution mass spectrometry	3
	1.4 Fourier-transform infrared spectroscopy	4
	1.5 Powder X-ray diffraction	4
	1.6 Nitrogen adsorption isotherm	4
	1.7 UV-Vis absorption spectra	4
	1.8 Photoluminescence	4
	1.9 Photo Yield Spectroscopy	4
	1.10 Thermogravimetric analysis	4
	1.11 Scanning electron microscopy	4
	1.12 Electron paramagnetic resonance spectroscopy	5
	1.13 Structure modeling, packing and band structures of COFs	5
	1.14 Apparent quantum yield	5
2.	Synthesis of the building blocks	6
3.	Synthesis of COFs	9
4.	Additional Figures	16

5.	Table	27
6.	References	28

1. Materials and methods

All the chemical reagents and solvents for the syntheses and photocatalytic hydrogen evolution were purchased from Tokyo Chemical Industry (TCI), Sigma Aldrich, Wako or Alfa Aesar and used without any further purification. The respective aldehyde and amine functionalized ligands were synthesized and purified in accordance with previous literature reports and modified accordingly to improve the yields.

1.1 Solution state nuclear magnetic resonance

^1H and ^{13}C NMR spectra were obtained in chloroform-*d* (CDCl_3), THF-*d*8, DMSO-*d*6 and acetone-*d*6 using TMS (0 ppm for ^1H) or CDCl_3 (77 ppm for ^{13}C) as an internal standard, recorded on a JEOL JNM-AL400 FT-NMR (^1H : 400 MHz; ^{13}C : 100 MHz) spectrometer.

1.2 Solid state nuclear magnetic resonance

Solid-state magic angle spinning (MAS) ^{13}C NMR measurements were performed using a Bruker Avance III 400 MHz spectrometer operating under a static field of 9.4 T. A double resonance probe with a 4.0 mm MAS probe head was used. For cross polarization (CP) MAS experiments, ^1H and ^{13}C field strengths of 55.6 kHz were used for the CP process, and the contact time was 1 ms. SPINAL 64 ^1H dipolar decoupling with a ^1H field strength of 62.5 kHz was applied during the detection of free induction decay. The dipolar dephasing MAS spectra, which selectively provide the resonance lines of quaternary carbons, were measured with a ^1H – ^{13}C dipolar dephasing time of 1.8 ms and a 180° pulse was applied in the middle of the dephasing time. The ^{13}C chemical shifts were expressed as values relative to tetramethylsilane using the $-\text{CH}_2$ resonance peak at 38.3 ppm for adamantane as an external reference. The MAS

spinning speed was set to 12 kHz and the experiments were conducted at 300 K. The –CH carbon spectra obtained by subtracting quaternary carbon spectra from the all carbon spectra.

1.3 High resolution mass spectrometry

High resolution mass spectra (HRMS) were obtained on a Thermo Fisher Exactive mass spectrometer.

1.4 Fourier-transform infrared spectroscopy

Fourier-Transform Infrared (FT-IR) spectra were recorded on a JASCO FT-IR 4700 instrument. Solid samples were directly placed and analyzed for 512 scans.

1.5 Powder X-ray diffraction

Powder X-ray diffraction (PXRD) measurements were carried out using a Rigaku MiniFlex 600 (Bragg–Brentano geometry, Cu K α radiation $\lambda = 1.54 \text{ \AA}$) instrument. Solid samples were placed uniformly over a glass sample holder and data was collected in reflection mode. Background correction was performed using the empty sample holder and subtracted from the sample.

1.6 Nitrogen adsorption isotherm

Adsorption isotherms of N₂ at 77 K were measured with Bellsorp-mini II equipment. Before the adsorption measurements, powdered samples were placed under reduced pressure ($<10^{-5}$ bar) at 120 °C for 12 h. For the evaluation of the surface area, the BET model was applied in the ranges $0.05 \leq p/p_0 \leq 0.25$.

1.7 UV-Vis absorption spectra

Diffuse reflectance spectra were measured on a JASCO V-650 UV-Vis spectrophotometer referenced to barium sulfate powder as white standard.

1.8 Photoluminescence

Solid state fluorescence was measured using JASCO FP-8500 spectrophotometer under ambient condition.

1.9 Photo Yield Spectroscopy

Photoelectron yield spectroscopy (PYS) measurements were conducted by using a Bunko Keiki BIP-KV202GD.

1.10 Thermogravimetric analysis

Thermogravimetric (TGA) analysis were performed on SHIMADZU DTG-60 instrument by heating the powder samples at a rate of 10 °C min⁻¹ under nitrogen gas flow in an open platinum pan to 900 °C.

1.11 Scanning electron microscopy

Morphological analysis of the COFs was performed using a JEOL JSM-7001F scanning electron microscope (SEM). Powder samples were placed over clean silicon wafer and imaged under high vacuum.

1.12 Electron paramagnetic resonance (EPR) spectroscopy

EPR spectra were acquired at room temperature under ambient conditions using a JEOL JES-FA200 X-band spectrometer. COF powders were taken in EPR tube and excited with xenon lamp (Hamamatsu, Lightningcure, LC8).

1.13 Structure modeling and band structure calculation of COFs

Using the Universal Force Field (UFF) as implement in the Amsterdam Modeling Suite (AMS) by SCM BV, bulk structures of **AntCOF**, **TpCOF**, and **TzCOF** were fully optimized (atomic positions and lattice vectors) using 1x1x4 super cells.¹ AB and ABC stackings were considered for **AntCOF**, whereas for **TpCOF** and **TzCOF**, AA', AB, and ABC stacking were taken into account. Steric hindrance prohibits the AA and AA' stackings in **AntCOF**.² Self-consistent

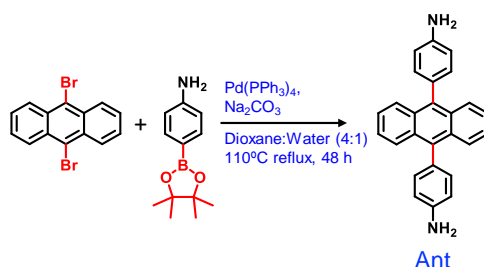
charge density functional based tight-binding (SCC-DFTB) method was employed to fully optimize the geometry of **BtCOF** with all the stacking arrangements using the DFTB+ code (1x1x4 super cell, Γ -point approximation, 3ob-3-1 parameters) with the UFF dispersion correction.³⁻⁶ This COF was selected for the DFTB level (higher level of theory than UFF), because it exhibits the best photoconductivity effects in our experiments and thus its electronic structure was of interest. PXRD data were simulated using the VESTA visualization program.⁷ Effective masses were calculated from the band edges of the electronic band structures, as the reversed of the band curvature at the given k point and fitting to a parabola. Refinements of PXRD pattern were done using Reflex module of Material studio.⁸ All the density functional theory (DFT) calculations in this study were carried out using B3LYP hybrid functional and the zeta basis set with polarization functions as implemented in the Gaussian09 suite (Revision D.01).⁹

1.13 Apparent quantum yield

The apparent quantum efficiency (AQE) of COFs was calculated using the following equation:

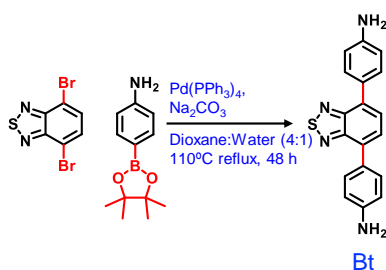
$$\text{AQE} = \frac{2 \times \text{number of hydrogen molecules}}{\text{number of incident photons}} \times 100$$

2. Synthesis of the building blocks



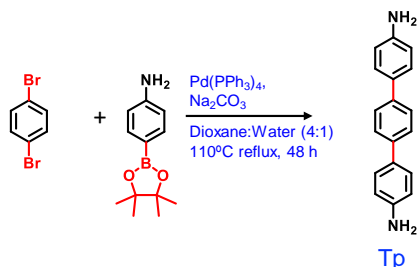
Synthesis of 4,4'-(anthracene-9,10-diyl)dianiline (Ant): Compound Ant was synthesized according to a previously published procedure.¹⁰ A mixture of 9,10-dibromoanthracene (500 mg, 1.49 mmol, 1 equiv), 4-aminophenylboronic acid pinacol ester (820 mg, 3.74 mmol, 2.5 equiv) and Na_2CO_3 (320 mg, 3.01 mmol, 2 equiv) in Dioxane/ H_2O (4:1, 50 mL) was degassed

with nitrogen for 15 minutes. $\text{Pd(PPh}_3)_4$ (160 mg, 0.14 mmol, 0.1 equiv) was added to the mixture and heated at 110 °C for 48 h under nitrogen. The reaction mixture was filtered through celite column to remove the palladium salt and the filtrate was diluted with dichloromethane. Then the organic layers were washed with water and dried over Na_2SO_4 . The solvent was evaporated under reduced pressure and the residue was purified by column chromatography (SiO_2) using hexane/chloroform (1:1) as eluent. The product was recrystallized from dichloromethane/hexane and the yellow crystals were washed with hexane. Yield: 300 mg (60 %). $^1\text{H-NMR}$ (400 MHz, chloroform-*d*, δ): 7.79 (m, 4H), 7.31 (m, 4H), 7.24 (d, $J = 8.4$ Hz, 4H), 6.91 (d, $J = 8.4$ Hz, 4H), 3.83 (s, 4H). $^{13}\text{C-NMR}$ (100 MHz, chloroform-*d*, δ): 145.6, 137.0, 132.2, 130.4, 129.0, 127.1, 124.6, 115.0. HRMS: 361.1657 $[\text{M}+\text{H}]^+$; Exact Mass: 360.16.

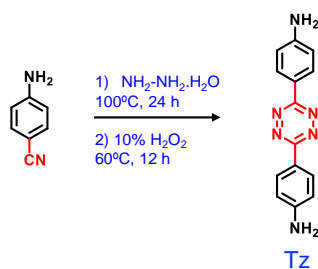


Synthesis of 4,4'-(benzo[c][1,2,5]thiadiazole-4,7-diyl)dianiline (Bt): A mixture of 4,7-dibromobenzo [c]-1,2,5-thiadiazole (500 mg, 1.71 mmol, 1 equiv), 4-aminophenylboronic acid pinacol ester (940 mg, 4.29 mmol, 2.5 equiv) and Na_2CO_3 (360 mg, 3.4 mmol, 2 equiv) in Dioxane/ H_2O (4:1, 50 mL) was degassed with nitrogen for 15 minutes. $\text{Pd(PPh}_3)_4$ (200 mg, 0.17 mmol, 0.1 equiv) was added to the mixture and heated at 110 °C for 24 h under nitrogen. The reaction mixture was filtered through celite column to remove the palladium salt and the filtrate was diluted with chloroform. Then the organic layers were washed with water and dried over Na_2SO_4 . The solvent was evaporated under reduced pressure and the residue was purified by column chromatography (SiO_2) using hexane/acetone (5:1) as eluent. The product was recrystallized from dichloromethane/acetone to give shiny orange-red crystals. Yield: 360 mg

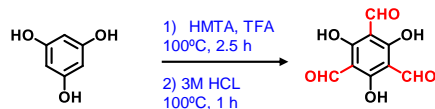
(66 %). $^1\text{H-NMR}$ (400 MHz, chloroform-*d*, δ): 7.82 (d, $J = 8.8$ Hz, 4H), 7.65 (s, 2H), 6.84 (d, $J = 8.8$ Hz, 4H), 3.81 (s, 4H). $^{13}\text{C-NMR}$ (100 MHz, chloroform-*d*, δ): 154.3, 146.7, 132.2, 130.2, 127.9, 126.9, 115.4. HRMS: 319.1948 $[\text{M}+\text{H}]^+$; Exact Mass: 318.09.



Synthesis of [1,1':4,1''-terphenyl]-4,4''-diamine (Tp): A mixture of 1,4-dibromobenzene (500 mg, 2.12 mmol, 1 equiv), 4-aminophenylboronic acid pinacol ester (1.16 g, 5.29 mmol, 2.5 equiv) and Na_2CO_3 (250 mg, 2.2 mmol, 2 equiv) in Dioxane/ H_2O (4:1, 50 mL) was degassed with nitrogen for 15 minutes. $\text{Pd}(\text{PPh}_3)_4$ (240 mg, 0.21 mmol, 0.1 equiv) was added to the mixture and heated at 110 °C for 24 h under nitrogen. The reaction mixture was filtered through celite column to remove the palladium salt and the filtrate was diluted with chloroform. Then the organic layers were washed with water and dried over Na_2SO_4 . The solvent was evaporated under reduced pressure and the residue was purified by column chromatography (SiO_2) using hexane/ethyl acetate (1:1) as eluent. The product was precipitated from acetone/hexane to give the required product as a pale-white solid. Yield: 270 mg (48 %). $^1\text{H-NMR}$ (400 MHz, $\text{DMSO-}d_6$, δ): 7.53 (d, $J = 8.4$ Hz, 4H), 7.39 (d, $J = 8.4$ Hz, 4H), 6.66 (d, $J = 8.4$ Hz, 4H), 5.20 (s, 4H). $^{13}\text{C-NMR}$ (100 MHz, $\text{DMSO-}d_6$, δ): 148.1, 137.9, 127.1, 126.8, 125.5, 114.2, 99.5. HRMS: 261.1393 $[\text{M}+\text{H}]^+$; Exact Mass: 260.13.



Synthesis of 4,4'-(1,2,4,5-tetrazine-3,6-diyl)dianiline (Tz): Two step synthetic procedure was adopted to synthesize Tz. Hydrazine monohydrate (98%, 5 mL) was added to crude 4-aminobenzonitrile (1.0 g, 8.4 mmol) and the solution was heated at 100 °C for 72 h. After cooling, the resulting orange-yellow precipitate was filtered, washed with water and immediately used in the next step without purification. Aqueous hydrogen peroxide (10%, 50 mL) was added to 3,6-bis-(4-aminophenyl)-1,2-dihydro-1,2,4,5- tetrazine (0.5 g, 1.8 mmol) and was warmed at 100 °C for 4 h. A red suspension was obtained, which was cooled and collected by filtration. The crude product was purified by column chromatography on silica gel using acetone and hexane (2:1) as eluent. Yield: 220 mg (40%). ¹H-NMR (400 MHz, DMSO-*d*₆, δ): 8.15 (d, *J* = 8.8 Hz, 4H), 6.73 (d, *J* = 8.8 Hz, 4H), 6.01 (s, 4H). ¹³C-NMR (100 MHz, DMSO-*d*₆, δ): 162.3, 152.8, 128.5, 118.3, 113.8. HRMS: 265.1201 [M+H]⁺; Exact Mass: 265.12.

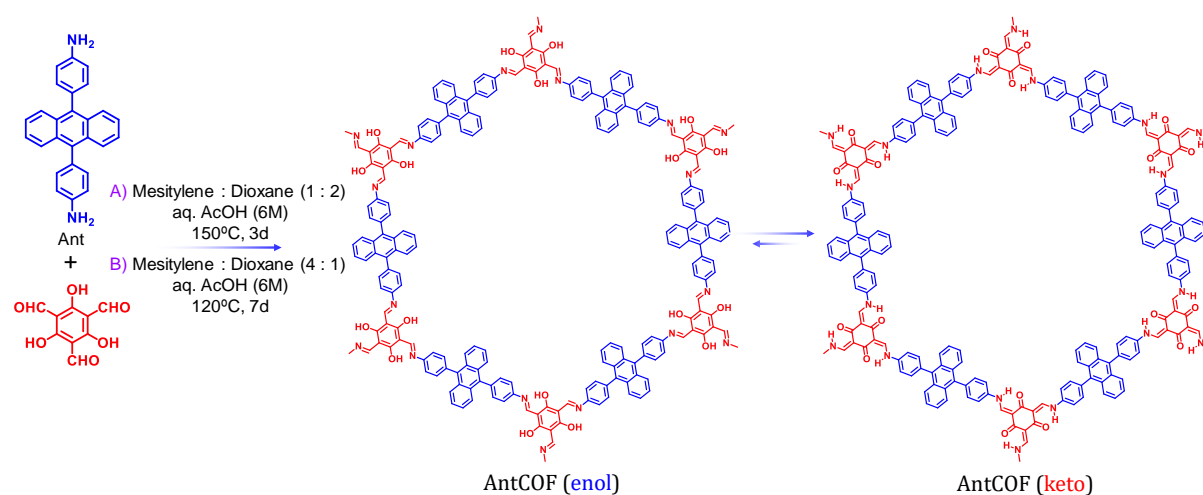


Synthesis of 2,4,6-trihydroxybenzene-1,3,5-tricarbaldehyde (TH):

To a mixture of hexamethylenetetraamine (15 g, 108 mmol) and phloroglucinol (6 g, 49 mmol), 90 mL trifluoroacetic acid was added under N₂. The mixture was heated at 100 °C for 3 h. After that 150 mL 3 M HCl was added to the mixture and the solution was again heated at 100 °C for 1 h. After cooling to room temperature, the solution was filtered through celite, extracted

with dichloromethane and dried over magnesium sulfate. Solvent was removed under reduced pressure which afforded an off-white powder which was then purified by column chromatography on silica gel using acetone and dichloromethane (2:1) as eluent. Yield: 1 g (10%). $^1\text{H-NMR}$ (400 MHz, chloroform-*d*, δ): 14.06 (s, 3H), 10.09 (s, 3H). $^{13}\text{C-NMR}$ (100 MHz, chloroform-*d*, δ): 192.0, 173.6, 102.9. HRMS: 211.1019 $[\text{M}+\text{H}]^+$; Exact Mass: 210.02.

3. Synthesis of COFs



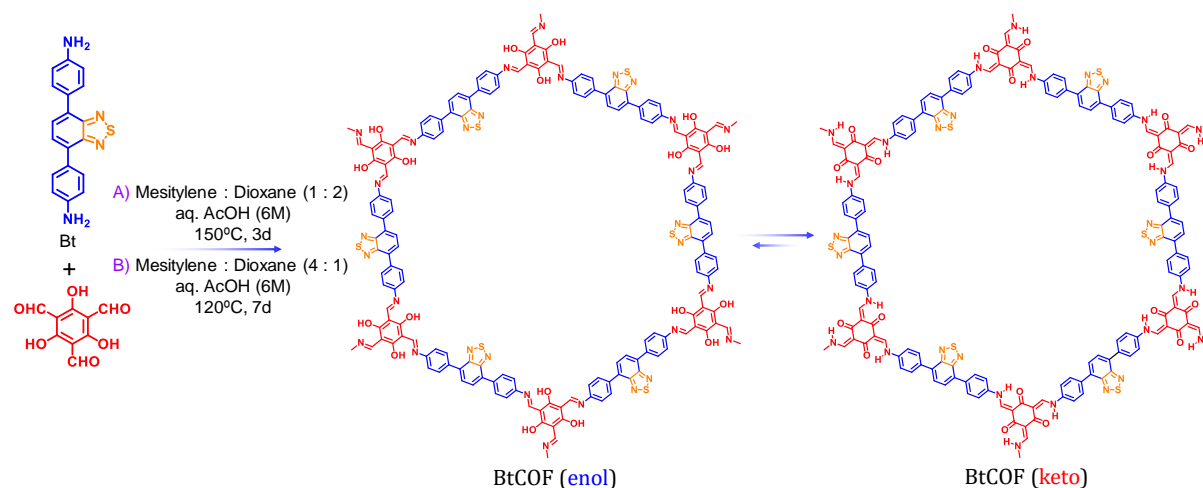
Synthesis of AntCOF150:

Ant (46.0 mg, 0.128 mM, 3 equiv.) and TH (18.0 mg, 0.086 mM, 2 equiv.) were taken in 20 mL BIOTAGE reaction tube, followed by the addition of mesitylene (2 mL), 1,4-dioxane (4 mL), and aqueous acetic acid (0.2 mL, 6 M). The reaction mixture was homogenized by sonication. The tube was sealed after purging nitrogen and kept at 150 °C for 3 days in an oven. After cooling to room temperature, the yellow precipitate was collected by filtration and washed with anhydrous *N,N*-Dimethylacetamide (DMAC), tetrahydrofuran (THF) and acetone. To remove the monomer completely, the precipitate was washed several times with anhydrous THF and centrifuged, until supernatant became colorless and non-fluorescent. Finally, the

precipitate was solvent exchanged with anhydrous acetone and dried at 100 °C under reduced pressure, yielding bright yellow powder (40 mg, 67%).

Synthesis of AntCOF120:

Ant (46.0 mg, 0.128 mM, 3 equiv.) and TH (18.0 mg, 0.086 mM, 2 equiv.) were taken in 20 mL BIOTAGE reaction tube, followed by the addition of mesitylene (2.5 mL), 1,4-dioxane (0.625 mL), and aqueous acetic acid (0.3 mL, 6 M). The reaction mixture was homogenized by sonication. The tube was sealed after purging nitrogen and kept at 120 °C for 7 days in an oven. After cooling to room temperature, the yellow precipitate was collected by filtration and washed with anhydrous DMAC, THF and acetone. To remove the monomer completely, the precipitate was washed several times with anhydrous THF and centrifuged, until supernatant became colorless and non-fluorescent. Finally, the precipitate was solvent exchanged with anhydrous acetone and dried at 100 °C under reduced pressure, yielding bright yellow powder (45 mg, 75%).



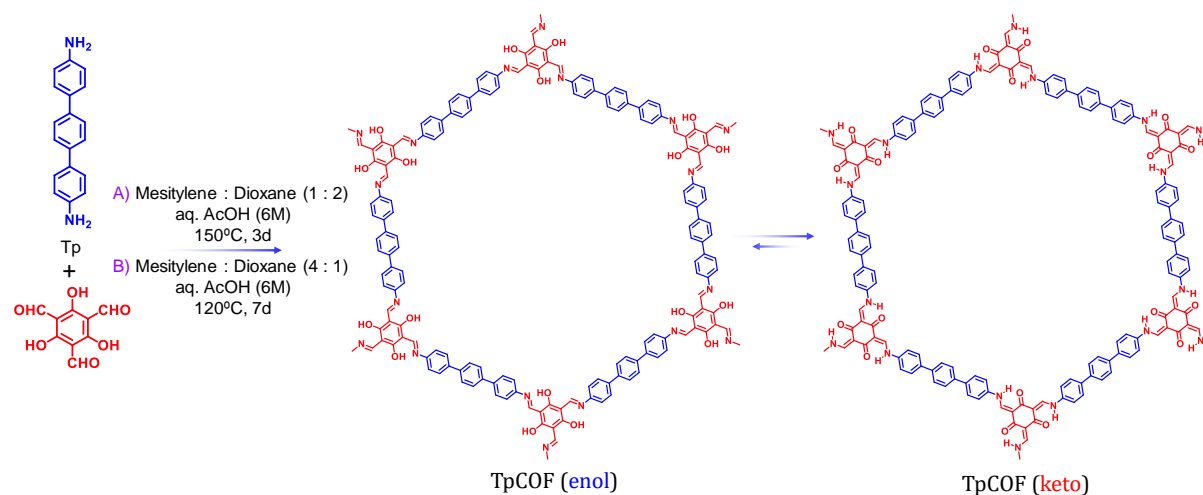
Synthesis of BtCOF150:

Bt (50.0 mg, 0.157 mM, 3 equiv.) and TH (22.0 mg, 0.105 mM, 2 equiv.) were taken in 20 mL BIOTAGE reaction tube, followed by the addition of mesitylene (2 mL), 1,4-dioxane (4 mL),

and aqueous acetic acid (0.4 mL, 6 M). The reaction mixture was homogenized by sonication. The tube was sealed after purging nitrogen and kept at 150 °C for 3 days in an oven. After cooling to room temperature, the red precipitate was collected by filtration and washed with anhydrous DMAC, THF and acetone. To remove the monomer completely, the precipitate was washed several times with anhydrous THF and centrifuged, until supernatant became colorless and non-fluorescent. Finally, the precipitate was solvent exchanged with anhydrous acetone and dried at 100 °C under reduced pressure, yielding bright red powder (60 mg, 90%).

Synthesis of BtCOF120:

Bt (50.0 mg, 0.157 mM, 3 equiv.) and TH (22.0 mg, 0.105 mM, 2 equiv.) were taken in 20 mL BIOTAGE reaction tube, followed by the addition of mesitylene (2.5 mL), 1,4-dioxane (0.625 mL), and aqueous acetic acid (0.3 mL, 6 M). The reaction mixture was homogenized by sonication. The tube was sealed after purging nitrogen and kept at 120 °C for 7 days in an oven. After cooling to room temperature, the red precipitate was collected by filtration and washed with anhydrous DMAC, THF and acetone. To remove the monomer completely, the precipitate was washed several times with anhydrous THF and centrifuged, until supernatant became colorless and non-fluorescent. Finally, the precipitate was solvent exchanged with anhydrous acetone and dried at 100 °C under reduced pressure, yielding bright red powder (56 mg, 84%).



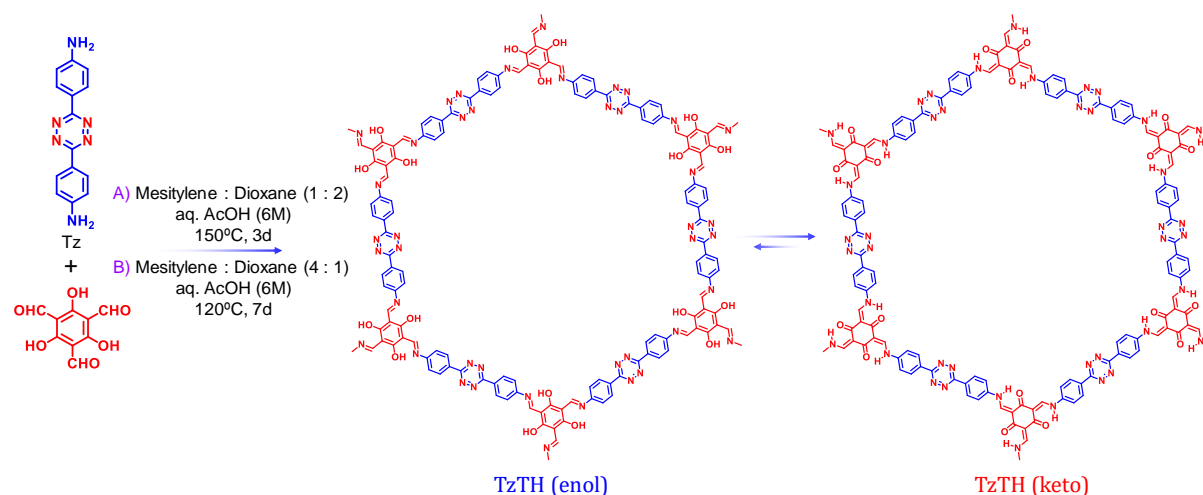
Synthesis of TpCOF150:

Tp (39.0 mg, 0.15 mM, 3 equiv.) and TH (21.0 mg, 0.10 mM, 2 equiv.) were taken in 20 mL BIOTAGE reaction tube, followed by the addition of mesitylene (2 mL), 1,4-dioxane (4 mL), and aqueous acetic acid (0.2 mL, 6 M). The reaction mixture was homogenized by sonication. The tube was sealed after purging nitrogen and kept at 150 °C for 3 days in an oven. After cooling to room temperature, the yellow precipitate was collected by filtration and washed with anhydrous DMAC, THF and acetone. To remove the monomer completely, the precipitate was washed several times with anhydrous THF and centrifuged, until supernatant became colorless and non-fluorescent. Finally, the precipitate was solvent exchanged with anhydrous acetone and dried at 100 °C under reduced pressure, yielding yellow powder (42 mg, 74%).

Synthesis of TpCOF120:

Tp (39.0 mg, 0.15 mM, 3 equiv.) and TH (21.0 mg, 0.10 mM, 2 equiv.) were taken in 20 mL BIOTAGE reaction tube, followed by the addition of mesitylene (2.5 mL), 1,4-dioxane (0.625 mL), and aqueous acetic acid (0.3 mL, 6 M). The reaction mixture was homogenized by sonication. The tube was sealed after purging nitrogen and kept at 120 °C for 7 days in an oven. After cooling to room temperature, the yellow precipitate was collected by filtration and

washed with anhydrous DMAC, THF and acetone. To remove the monomer completely, the precipitate was washed several times with anhydrous THF and centrifuged, until supernatant became colorless and non-fluorescent. Finally, the precipitate was solvent exchanged with anhydrous acetone and dried at 100 °C under reduced pressure, yielding yellow powder (44 mg, 78%).

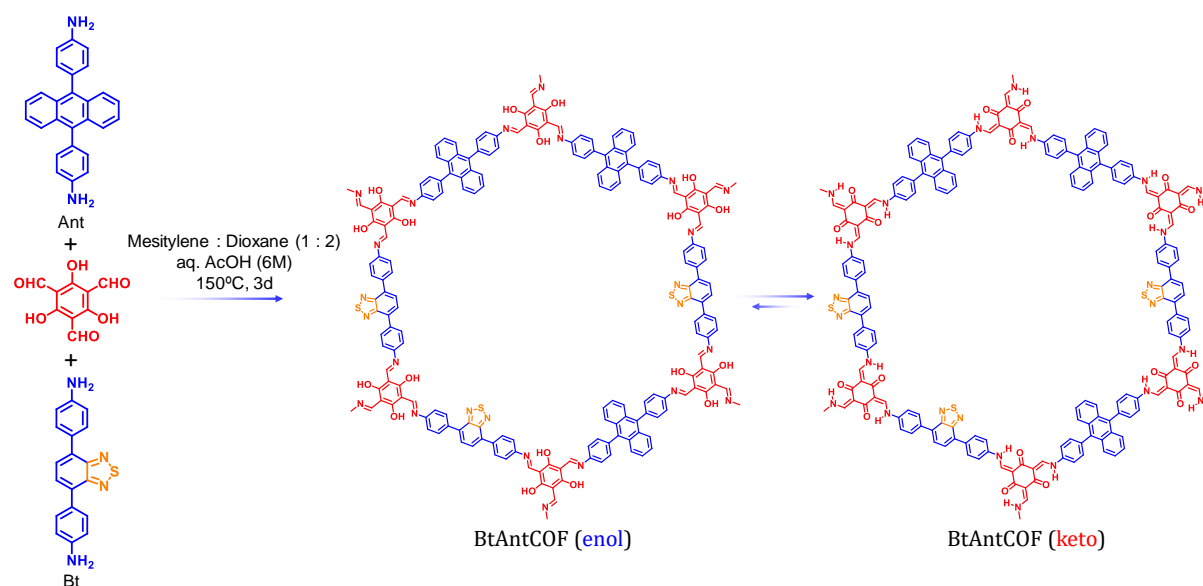


Synthesis of TzCOF150:

Tz (30.0 mg, 0.114 mM, 3 equiv.) and TH (16.0 mg, 0.076 mM, 2 equiv.) were taken in 20 mL BIOTAGE reaction tube, followed by the addition of mesitylene (2 mL), 1,4-dioxane (4 mL), and aqueous acetic acid (0.4 mL, 6 M). The reaction mixture was homogenized by sonication. The tube was sealed after purging nitrogen and kept at 150 °C for 3 days in an oven. After cooling to room temperature, the red precipitate was collected by filtration and washed with anhydrous DMAC, THF and acetone. To remove the monomer completely, the precipitate was washed several times with anhydrous DMAC and centrifuged, until supernatant became colorless. Finally, the precipitate was solvent exchanged with anhydrous acetone and dried at 100 °C under reduced pressure, yielding yellow powder (36 mg, 84%).

Synthesis of TzCOF120:

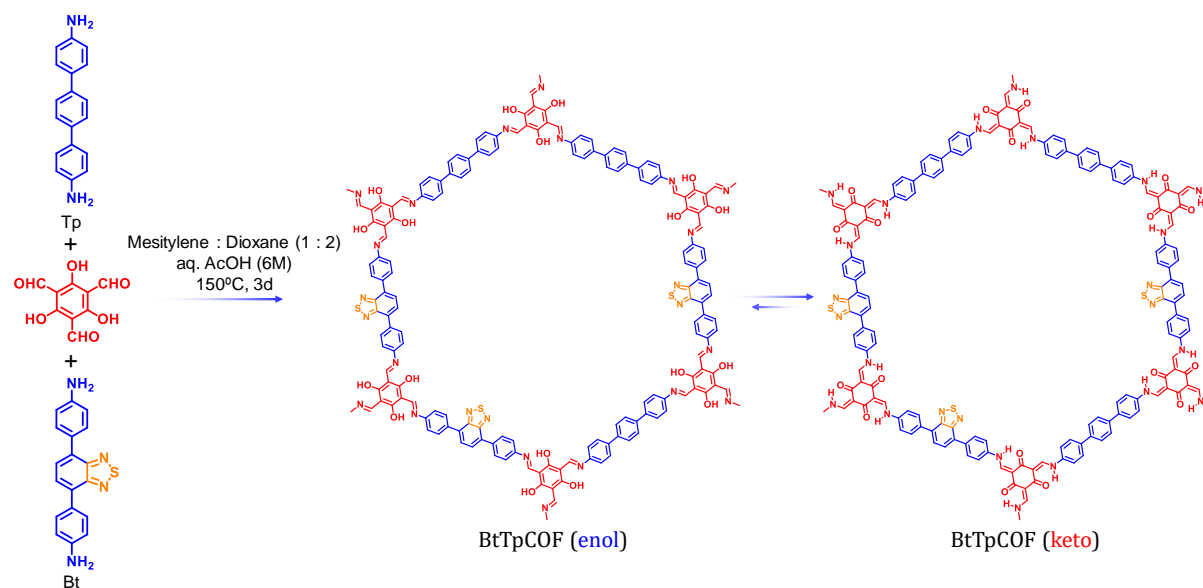
Tz (30.0 mg, 0.114 mM, 3 equiv.) and TH (16.0 mg, 0.10 mM, 2 equiv.) were taken in 20 mL BIOTAGE reaction tube, followed by the addition of mesitylene (2.5 mL), 1,4-dioxane (0.625 mL), and aqueous acetic acid (0.3 mL, 6 M). The reaction mixture was homogenized by sonication. The tube was sealed after purging nitrogen and kept at 120 °C for 7 days in an oven. After cooling to room temperature, the yellow precipitate was collected by filtration and washed with anhydrous DMAC, THF and acetone. To remove the monomer completely, the precipitate was washed several times with anhydrous THF and centrifuged, until supernatant became colorless. Finally, the precipitate was solvent exchanged with anhydrous acetone and dried at 100 °C under reduced pressure, yielding yellow powder (30 mg, 70%).



Synthesis of BtAntCOF:

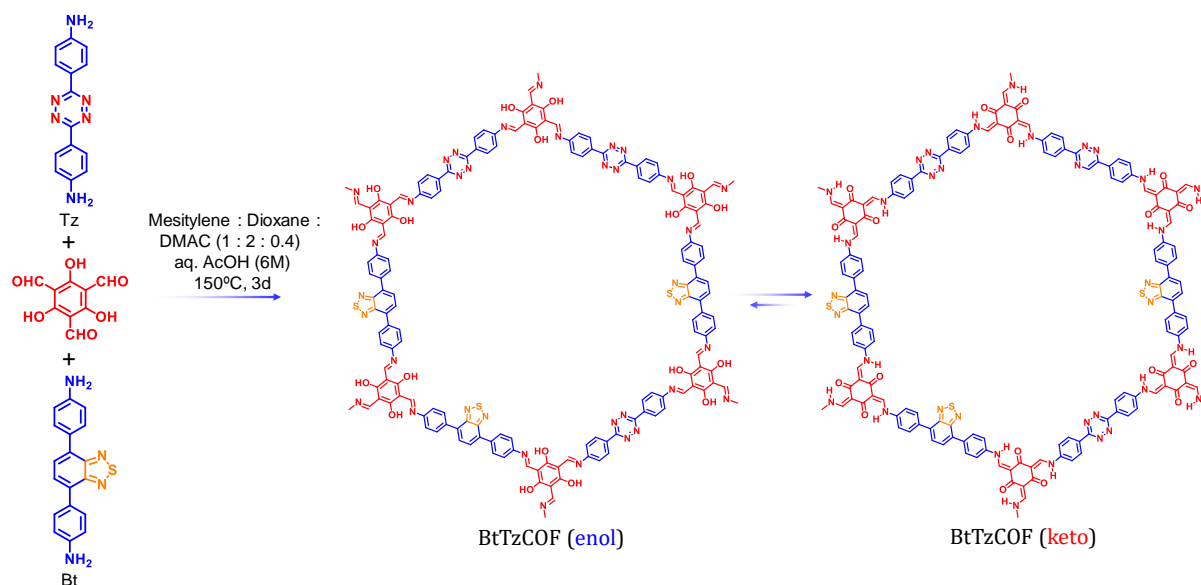
Ant (23.0 mg, 0.064 mM, 1.5 equiv.), Bt (20.3 mg, 0.064 mM, 1.5 equiv.) and TH (18.0 mg, 0.086 mM, 2 equiv) were taken in 20 mL BIOTAGE reaction tube, followed by the addition of mesitylene (2 mL), 1,4-dioxane (4 mL), and aqueous acetic acid (0.2 mL, 6 M). The reaction mixture was homogenized by sonication. The tube was sealed after purging nitrogen and kept at 150 °C for 3 days in an oven. After cooling to room temperature, the orange precipitate was collected by filtration and washed with anhydrous DMAC, THF and acetone. To remove the

monomer completely, the precipitate was washed several times with anhydrous THF and centrifuged, until supernatant became colorless and non-fluorescent. Finally, the precipitate was solvent exchanged with anhydrous acetone and dried at 100 °C under reduced pressure, yielding bright orange powder (38 mg, 68%).



Synthesis of BtTpCOF:

Tp (20.4 mg, 0.078 mM, 1.5 equiv.), Bt (25.0 mg, 0.078 mM, 1.5 equiv.) and TH (22.0 mg, 0.105 mM, 2 equiv) were taken in 20 mL BIOTAGE reaction tube, followed by the addition of mesitylene (2 mL), 1,4-dioxane (4 mL), and aqueous acetic acid (0.4 mL, 6 M). The reaction mixture was homogenized by sonication. The tube was sealed after purging nitrogen and kept at 150 °C for 3 days in an oven. After cooling to room temperature, the orange precipitate was collected by filtration and washed with anhydrous DMAC, THF and acetone. To remove the monomer completely, the precipitate was washed several times with anhydrous THF and centrifuged, until supernatant became colorless and non-fluorescent. Finally, the precipitate was solvent exchanged with anhydrous acetone and dried at 100 °C under reduced pressure, yielding bright orange powder (50 mg, 80%).



Synthesis of BtTzCOF:

Tz (20.7 mg, 0.078 mM, 1.5 equiv.), Bt (25.0 mg, 0.078 mM, 1.5 equiv.) and TH (22.0 mg, 0.105 mM, 2 equiv.) were taken in 20 mL BIOTAGE reaction tube, followed by the addition of mesitylene (2 mL), DMAC (0.5 mL), 1,4-dioxane (4 mL), and aqueous acetic acid (0.4 mL, 6 M). The reaction mixture was homogenized by sonication. The tube was sealed after purging nitrogen and kept at 150 °C for 3 days in an oven. After cooling to room temperature, the red precipitate was collected by filtration and washed with anhydrous DMAC, THF and acetone. To remove the monomer completely, the precipitate was washed several times with anhydrous DMAC and centrifuged, until supernatant became colorless and non-fluorescent. Finally, the precipitate was solvent exchanged with anhydrous acetone and dried at 100 °C under reduced pressure, yielding dark red powder (52 mg, 82%).

4. Additional Figures

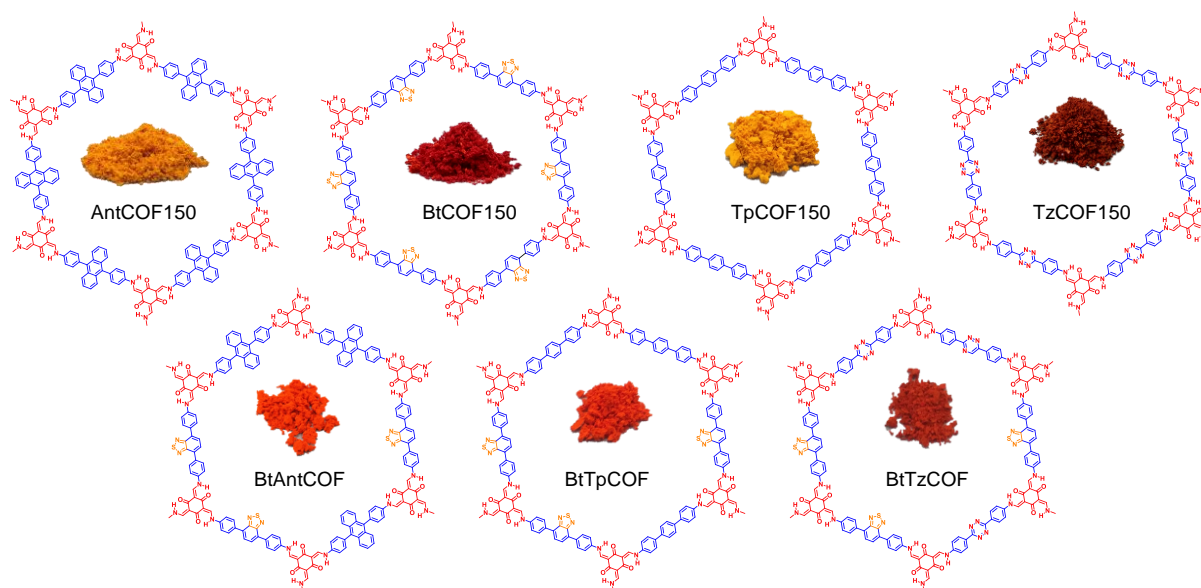


Figure S1. Chemical structure of COFs along with the photograph of COF powders under ambient light.

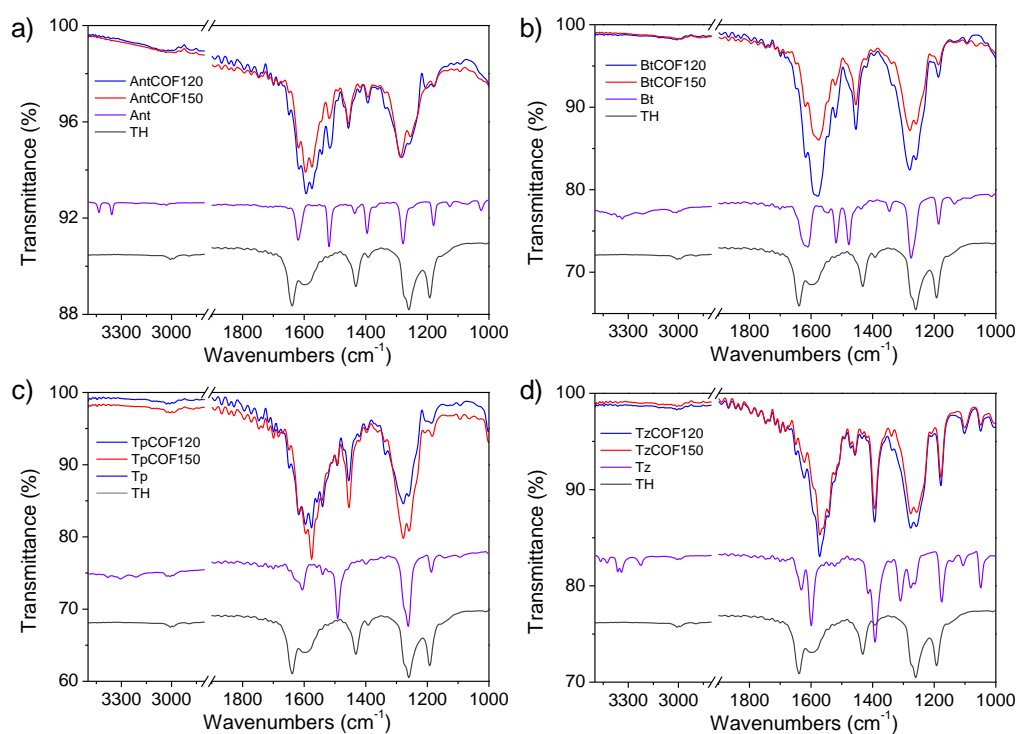


Figure S2. FT-IR spectra of a) **AntCOF150** and **AntCOF120**; b) **BtCOF150** and **BtCOF120**; c) **TpCOF150** and **TpCOF120**; d) **TzCOF150** and **TzCOF120**, along with their corresponding building blocks.

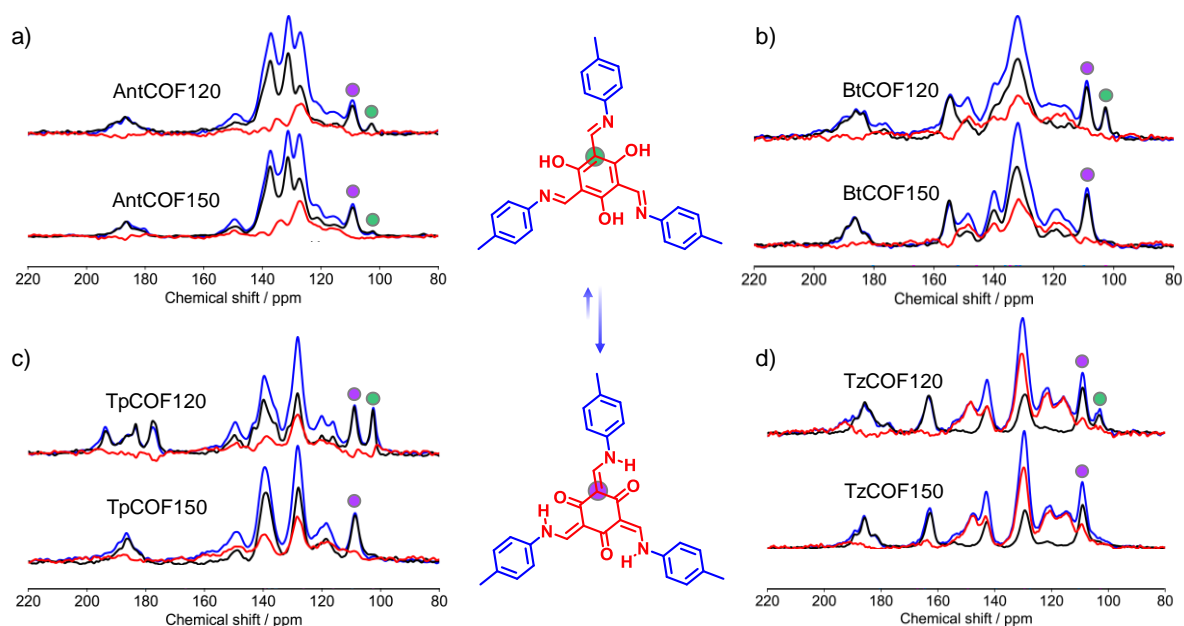


Figure S3. ^{13}C CP-MAS spectra of a) **AntCOF150** and **AntCOF120**; b) **BtCOF150** and **BtCOF120**; c) **TpCOF150** and **TpCOF120**; d) **TzCOF150** and **TzCOF120**. All carbons (—), quaternary carbons (—) and CH carbons (—).

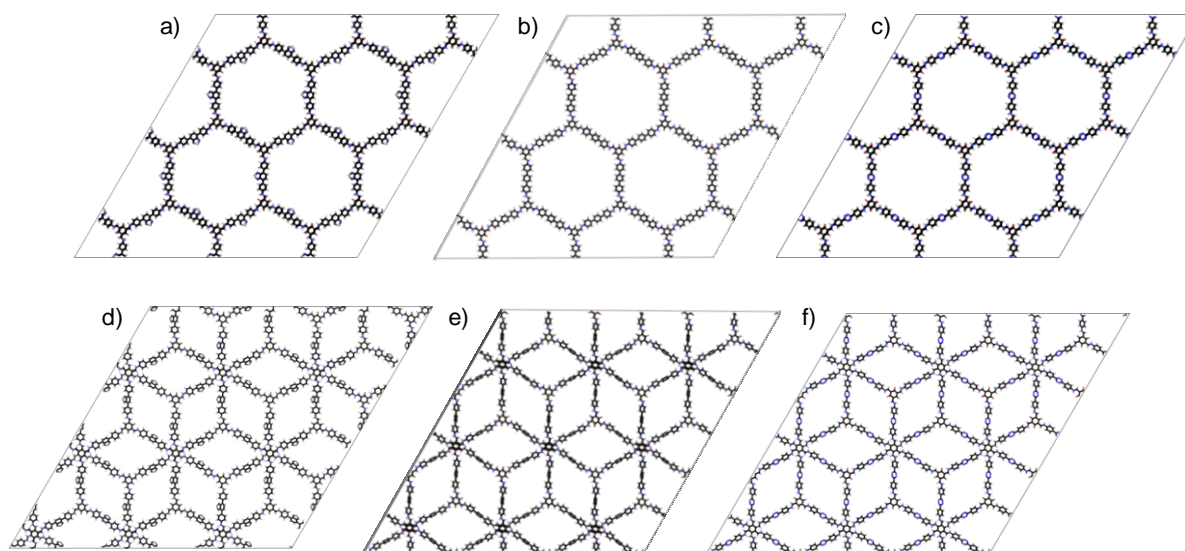


Figure S4. Supercell representations of AA' stacked a) **BtCOF**, b) **TpCOF** and c) **TzCOF**; AB stacked d) **BtCOF**, e) **TpCOF** and f) **TzCOF**.

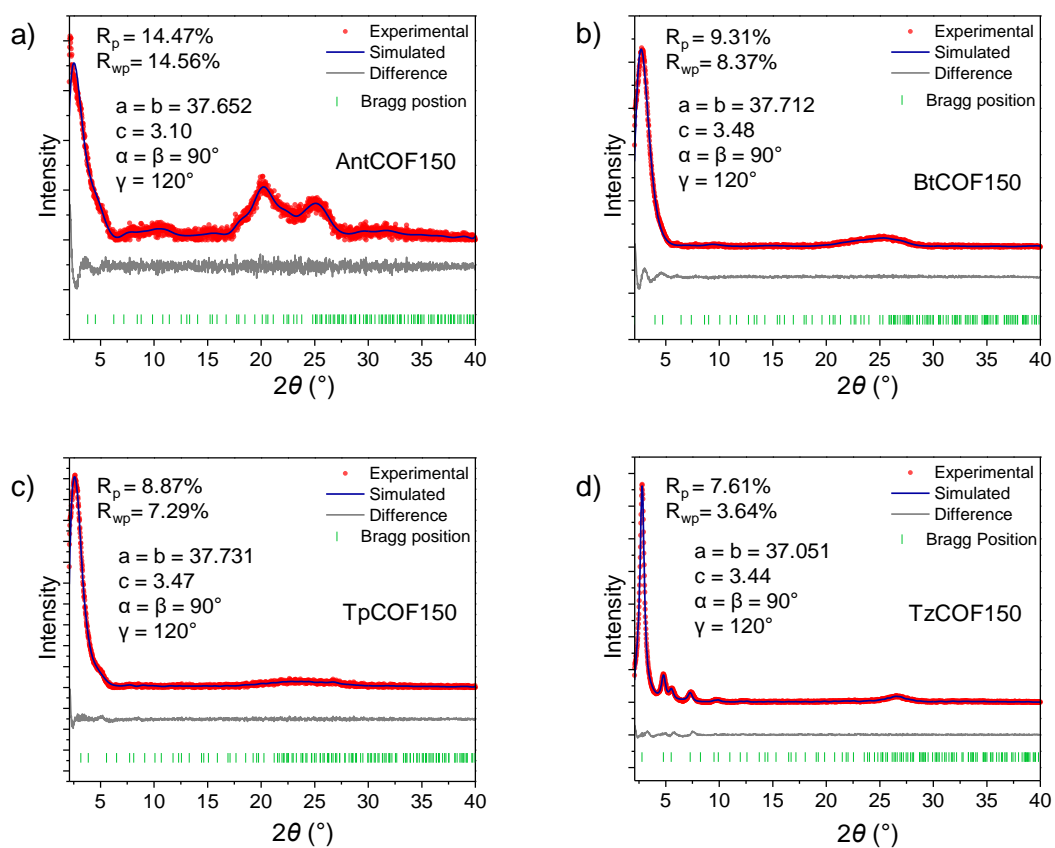


Figure S5. Pawley refinement of the PXRD of a) **AntCOF150**, b) **BtCOF150**, c) **TpCOF150** and d) **TzCOF150**.

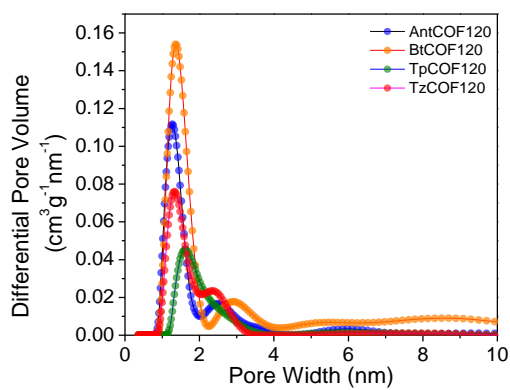


Figure S6. Pore size distribution of **AntCOF120**, **BtCOF120**, **TpCOF120** and **TzCOF120**.

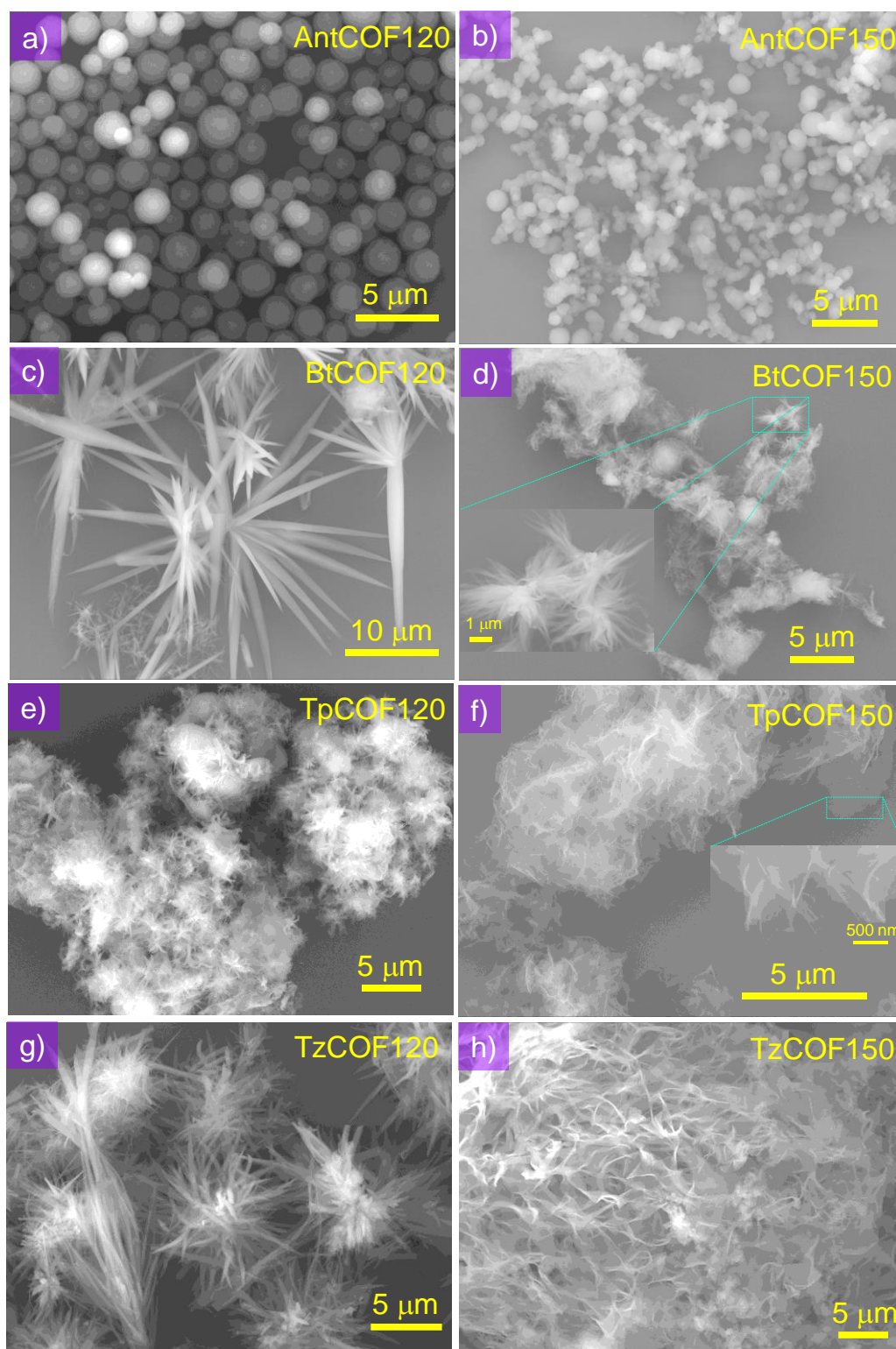


Figure S7. SEM images of a) **AntCOF120**, b) **AntCOF150**, c) **BtCOF120**, d) **BtCOF150**, e) **TpCOF120**, f) **TpCOF150**, g) **TzCOF120** and h) **TzCOF150**.

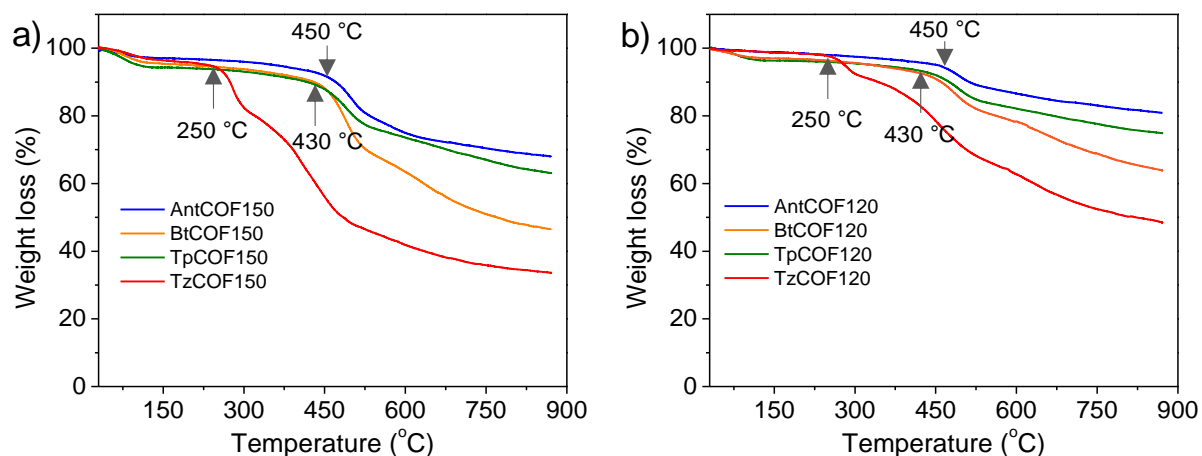


Figure S8. TGA profile of a) **AntCOF150**, **BtCOF150**, **TpCOF150** and **TzCOF150**; b) **AntCOF120**, **BtCOF120**, **TpCOF120** and **TzCOF120**.

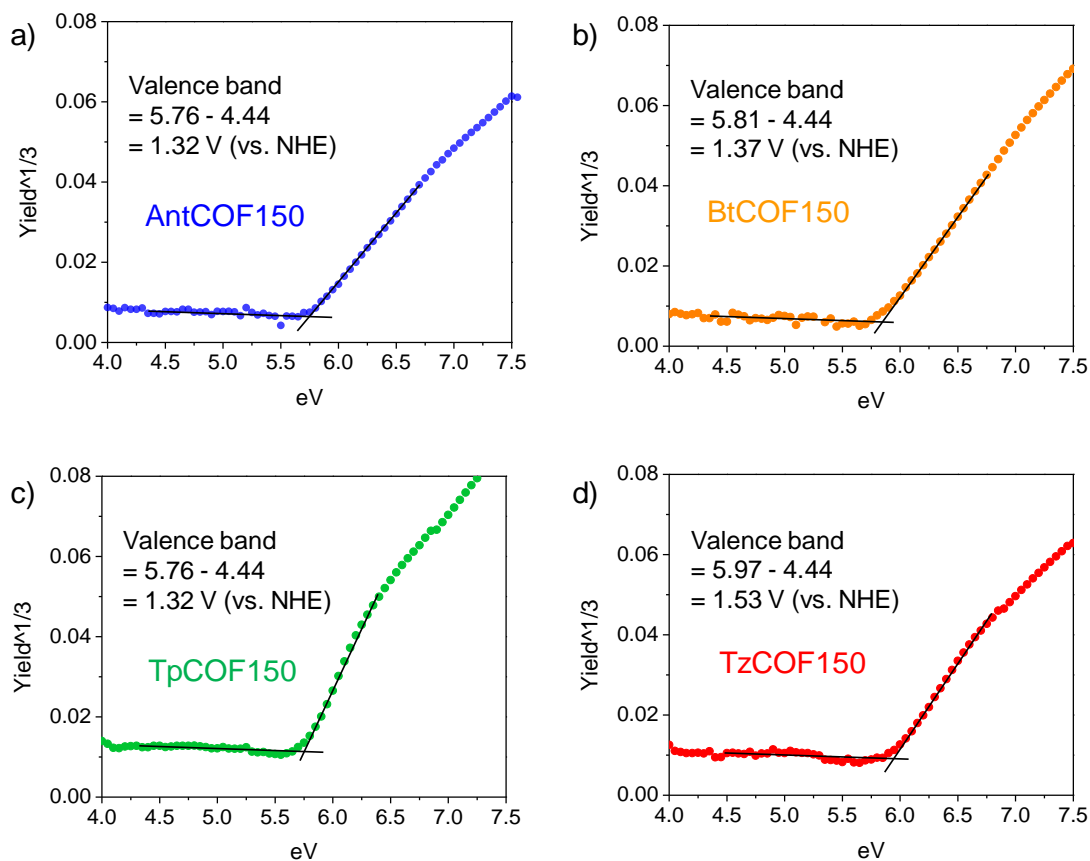


Figure S9. Photocatalytic activity (PYS) of a) **AntCOF150**, b) **BtCOF150**, c) **TpCOF150** and d) **TzCOF150** powders.

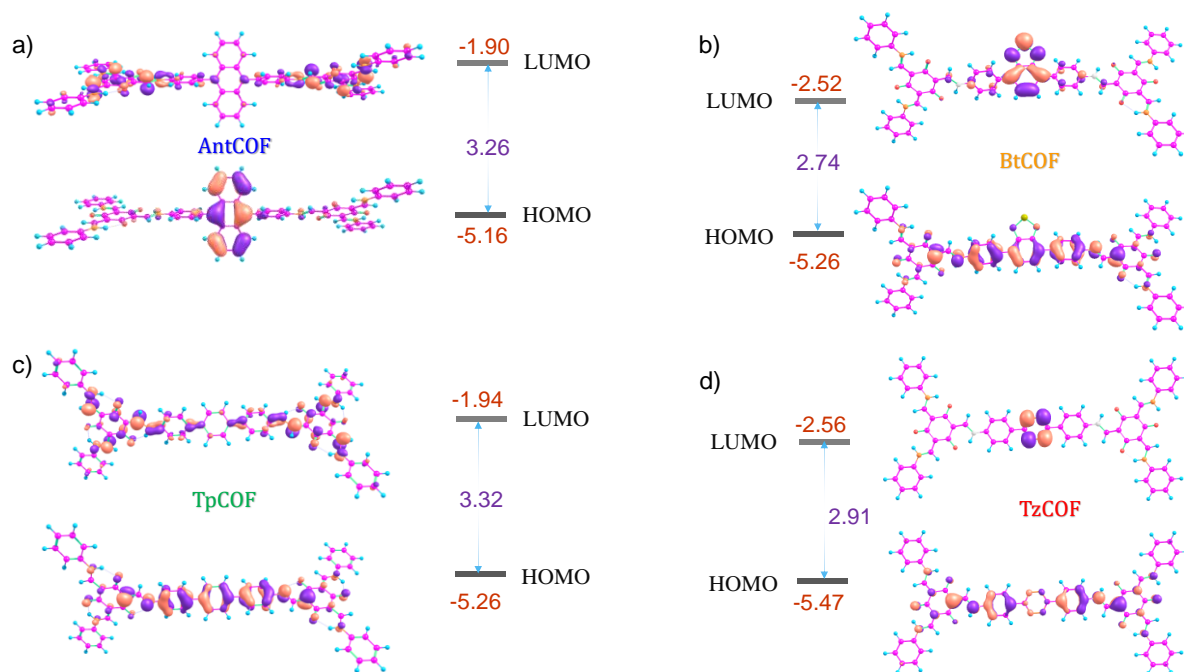


Figure S10. Frontier molecular orbitals and HOMO-LUMO energies of the smallest model unit of a) **AntCOF**, b) **BtCOF**, c) **TpCOF** and d) **TzCOF**.

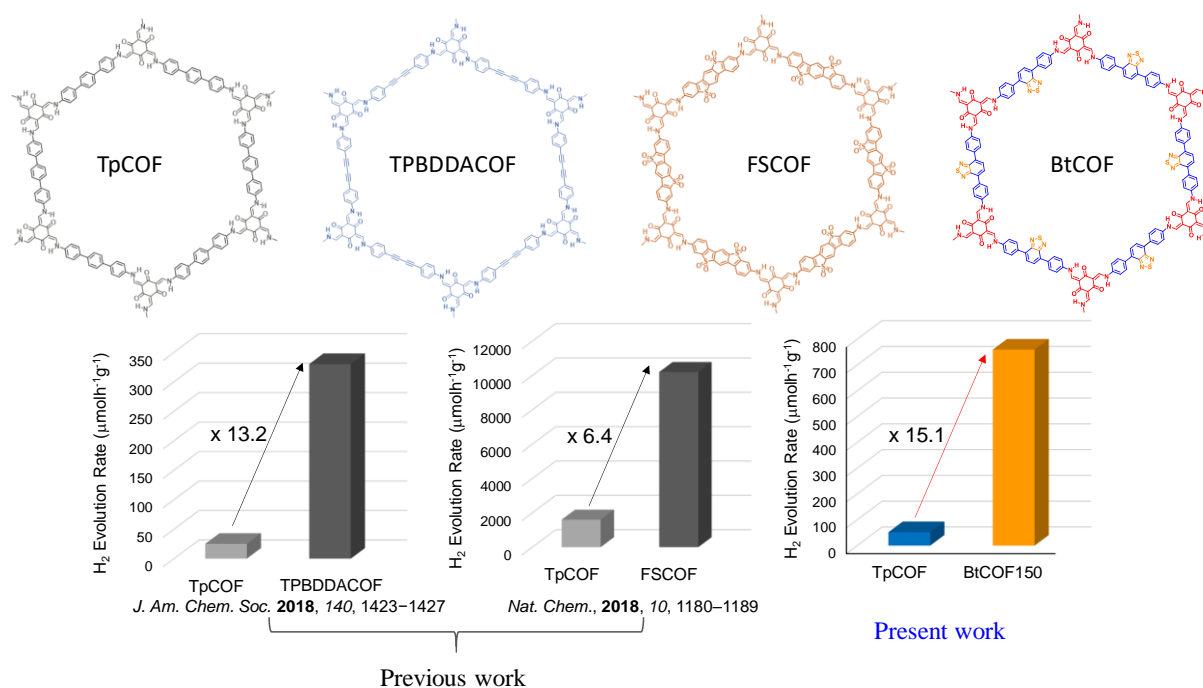


Figure S11. Comparison chart showing the rate of H_2 evolution with previous reports.

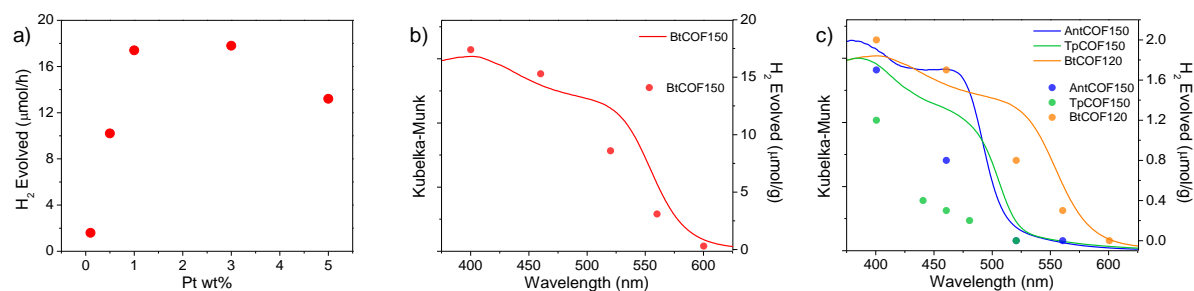


Figure S12. a) Variation in H_2 evolution with the increase in Pt wt% using same amount of BtCOF150. Wavelength dependent H_2 evolution of b) BtCOF150 and c) AntCOF150, TpCOF150 and BtCOF120, using bandpass filters.

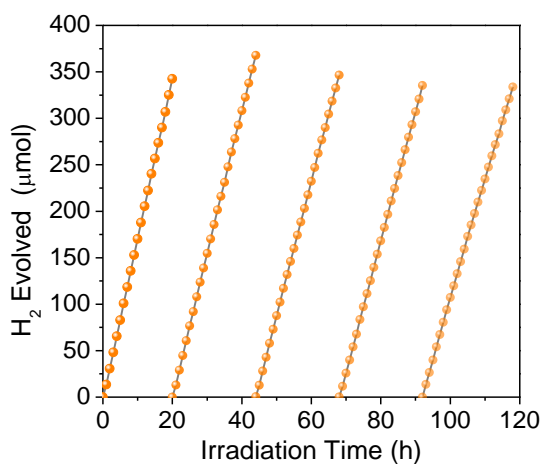


Figure S13. H_2 production analysis using visible light for BtCOF150 for over 120 h.

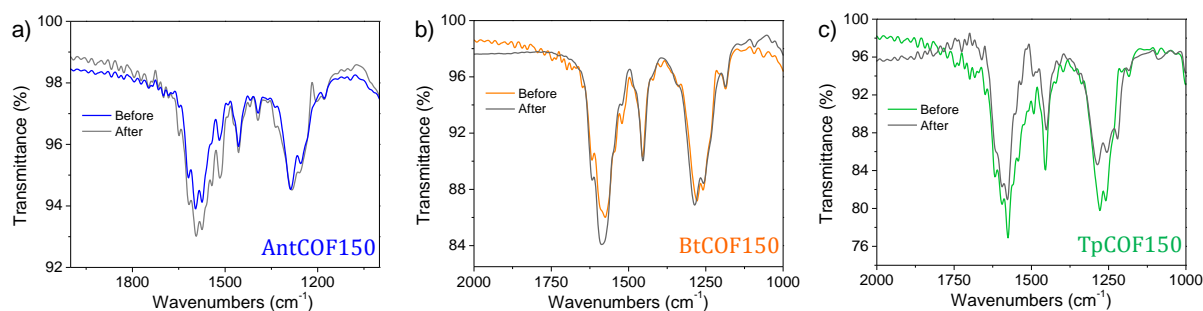


Figure S14. FT-IR spectra of a) AntCOF150, b) BtCOF150, c) TpCOF150, d) AntCOF120, e) BtCOF120 and f) TpCOF150 before and after photocatalysis of 24 h.

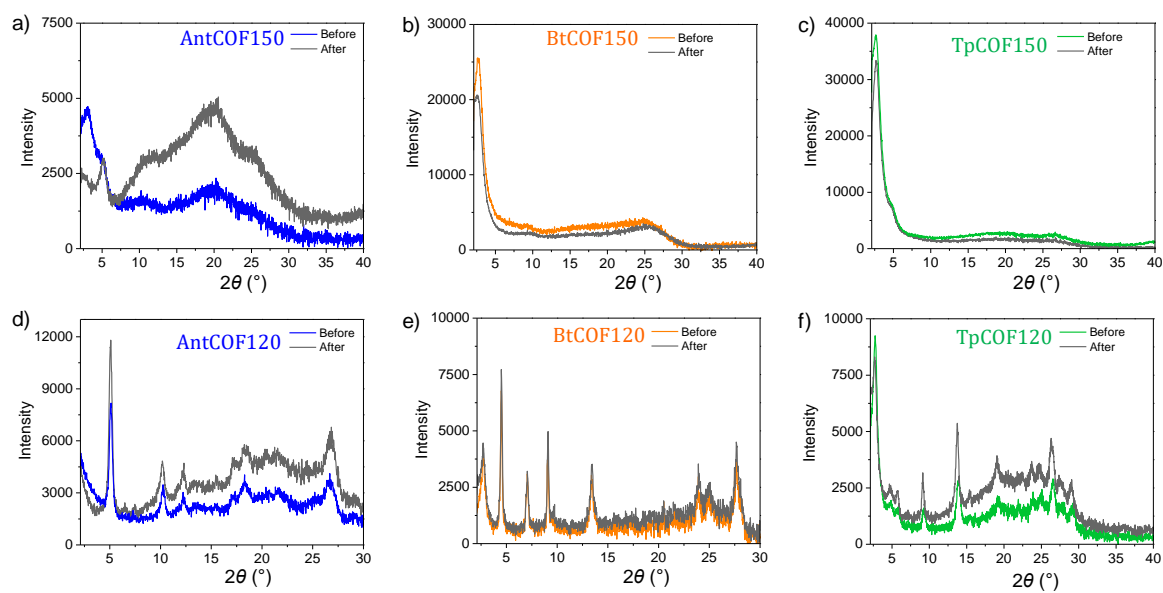


Figure S15. Experimental PXRD pattern of a) **AntCOF150**, b) **BtCOF150**, c) **TpCOF150**, d) **AntCOF120**, e) **BtCOF120** and f) **TpCOF120** before and after photocatalysis of 24 h.

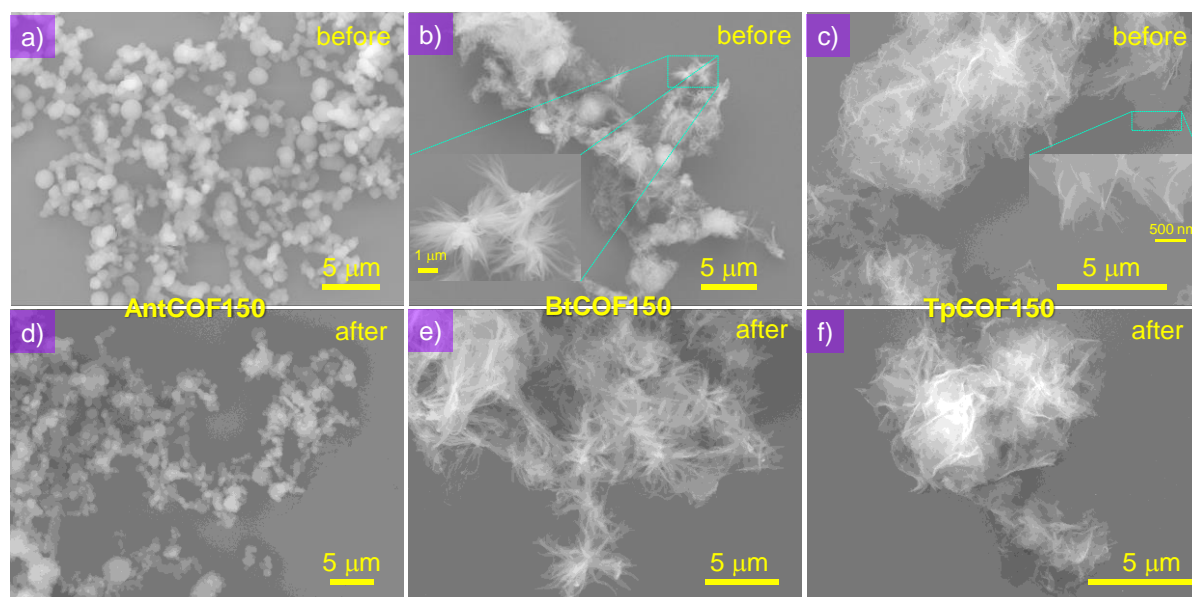


Figure S16. SEM images of a,d) **AntCOF150**, b,e) **BtCOF150** and c,f) **TpCOF150** before and after photocatalysis of 24 h.

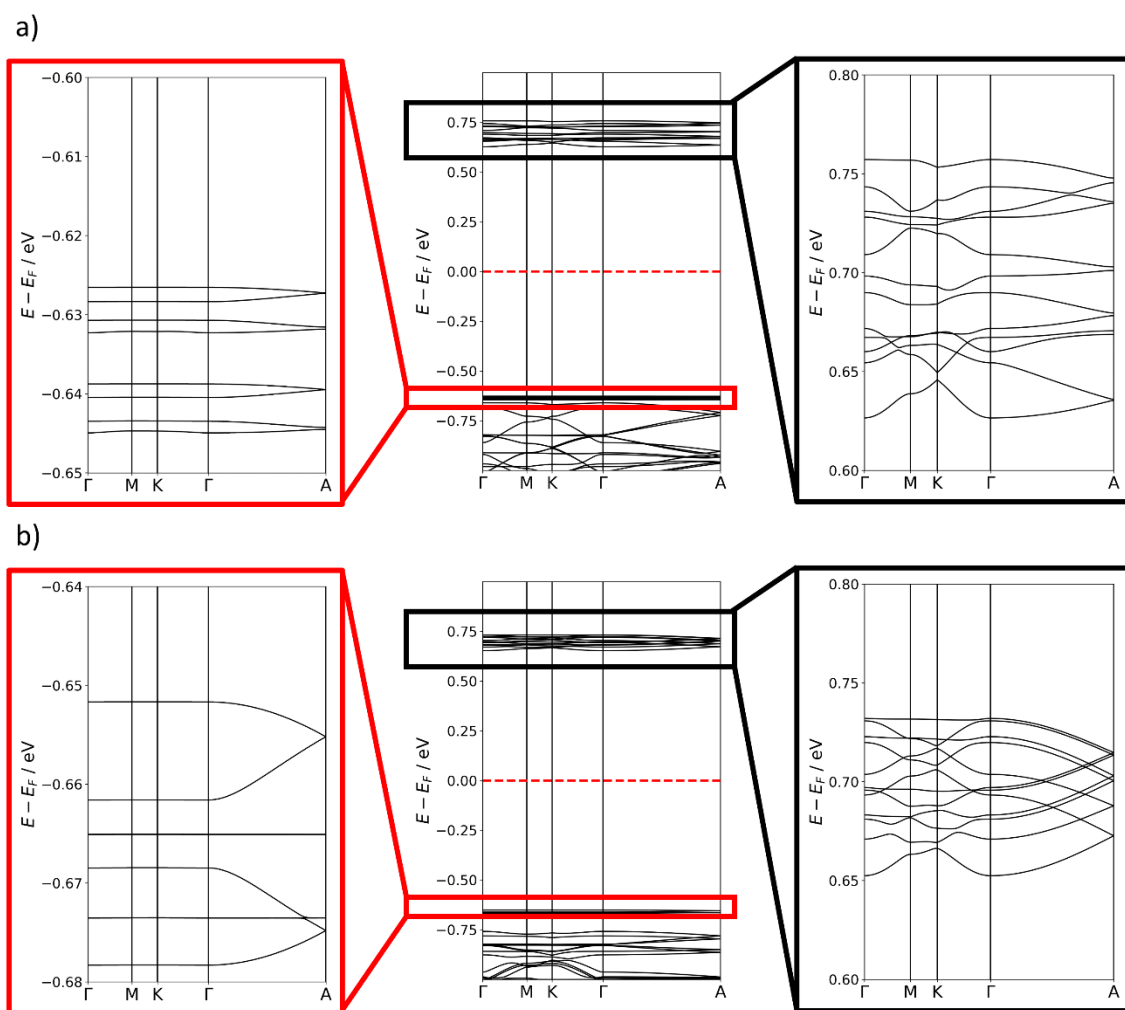


Figure S17. Band structures of **BtCOF** a) AA' stacked, and b) AB stacked along with simulated packing.

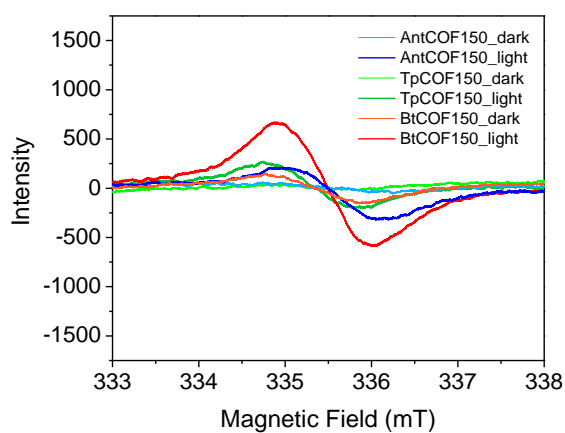


Figure S18. EPR spectra of pristine **AntCOF150**, **TpCOF150** and **BtCOF150**, in presence of light and dark.

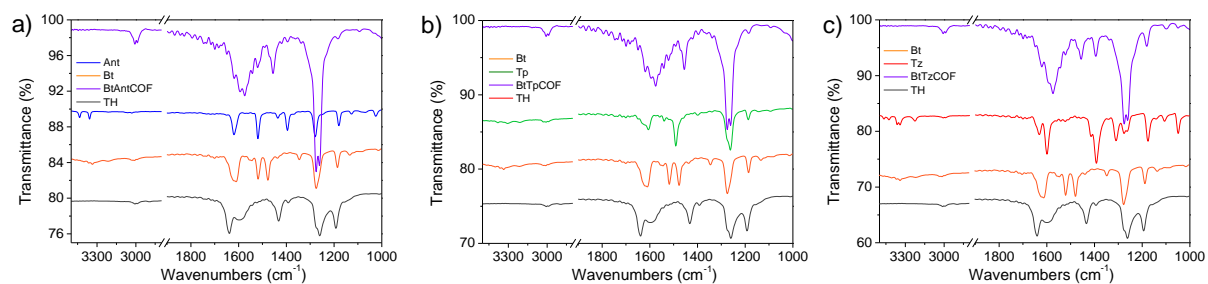


Figure S19. FT-IR spectra of a) **BtAntCOF**, b) **BtTpCOF** c) **BtTzCOF** and their corresponding building blocks.

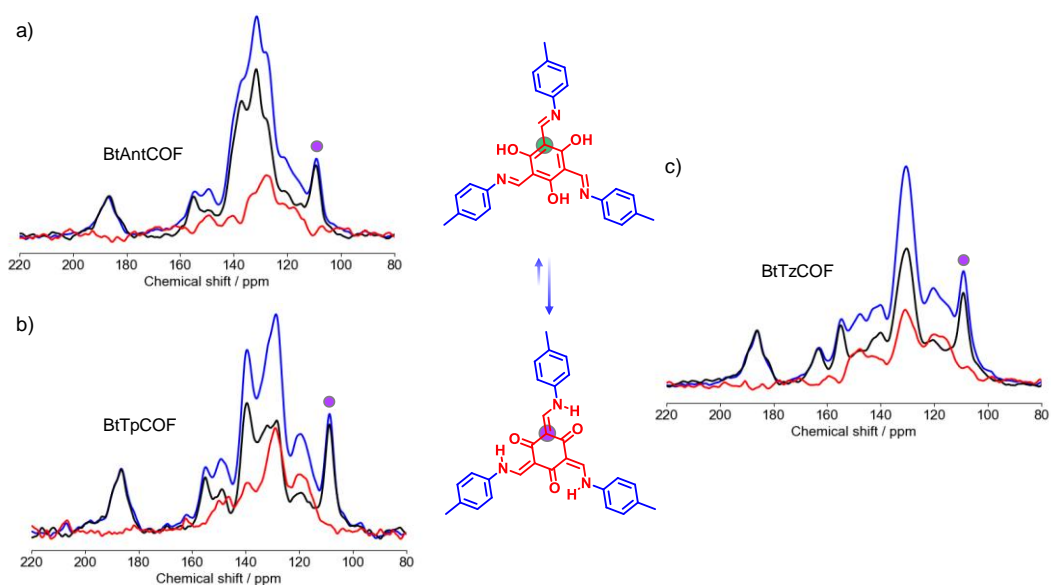


Figure S20. ^{13}C CP-MAS spectra of a) **BtAntCOF**, b) **BtTpCOF** and c) **BtTzCOF**. All carbons (—), quaternary carbons (—) and CH carbons (—).

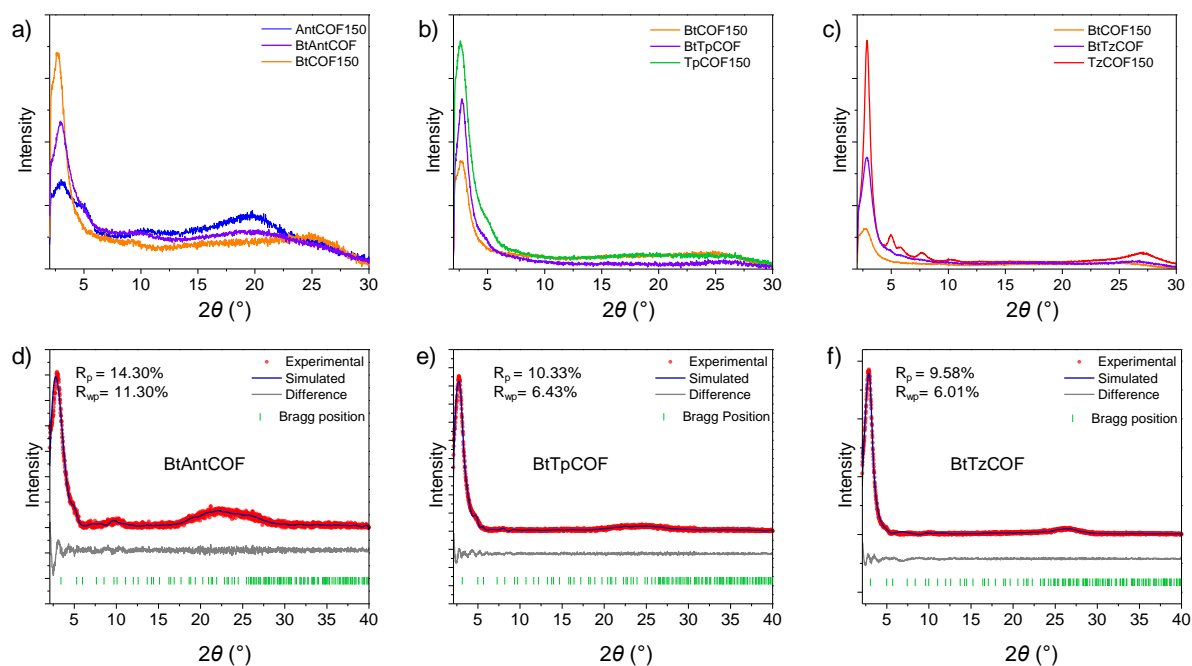


Figure S21. Experimental PXRD of a) **BtAntCOF**, b) **BtTpCOF** c) **BtTzCOF** and compared with the parent COFs. Pawley refinement of the PXRD of a) **BtAntCOF**, b) **BtTpCOF** and c) **BtTzCOF**.

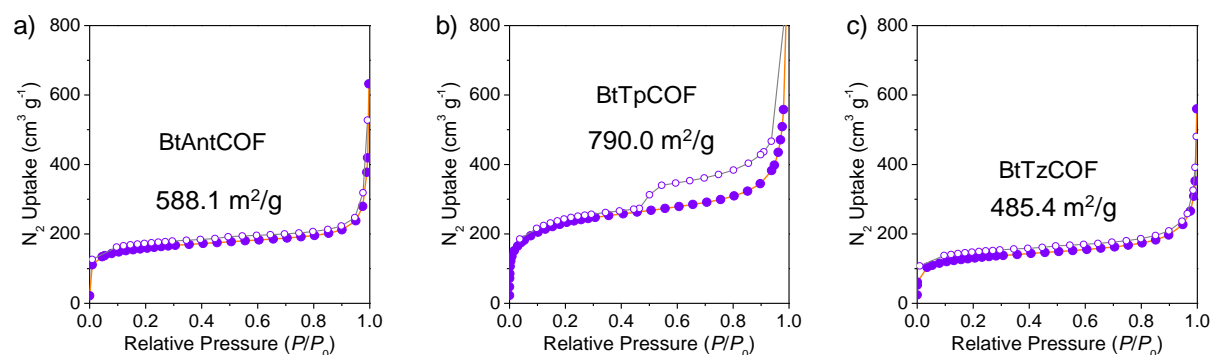


Figure S22. Nitrogen sorption isotherms at 77 K for a) **BtAntCOF**, b) **BtTpCOF** and c) **BtTzCOF** along with BET surface area. Adsorption and desorption denoted by filled and open circles respectively.

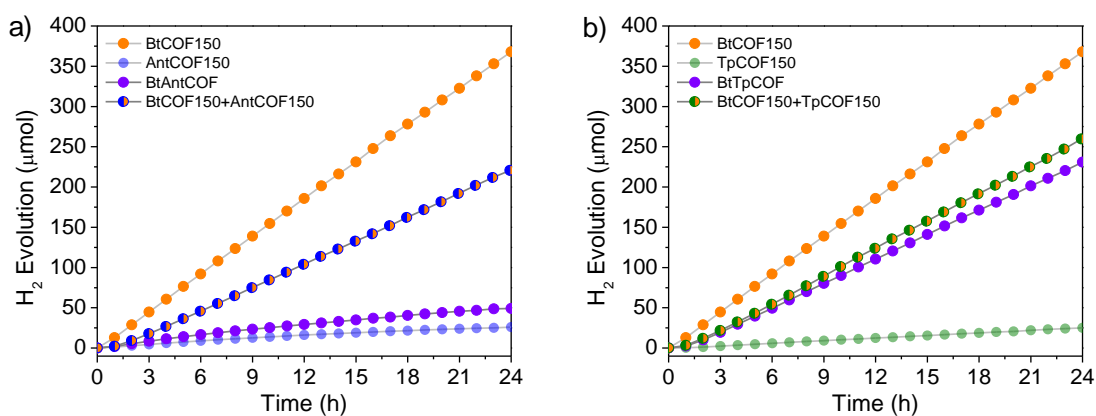


Figure S23. Time course for photocatalytic H₂ production using visible light for a) **BtCOF150**, **AntCOF150**, **BtAntCOF** and **BtCOF150+AntCOF150** (1:1 wt), b) **BtCOF150**, **TpCOF150**, **BtTpCOF** and **BtCOF150+TpCOF150** (1:1 wt).

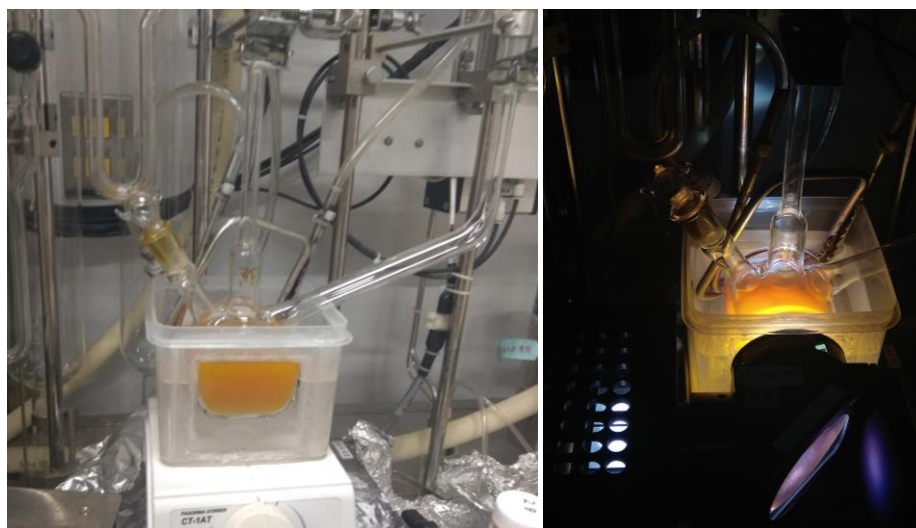


Figure S24. Photograph showing the photocatalytic reaction setup for H₂ evolution.

Table S1. Calculated effective masses of electrons (m^* / m_0) for three different stackings calculated from simulated bulk structures for **BtCOF**. This COF exhibits very heavy holes, due to nearly dispersionless top of the valence band.

Edge of Brillouin Zone	$\Gamma \rightarrow M$	$\Gamma \rightarrow K$	$\Gamma \rightarrow A$
BtCOF AA'	0.084	0.087	0.864
BtCOF AB	0.122	0.112	0.334

Table S2. Porosity, crystallinity, photophysical properties and rate of H₂ evolution of all the COFs.

COF	BET surface area (m ² g ⁻¹)	Degree of Crystallinity	Stacking	Light absorption	Bandgap (eV) ^c	Rate of H ₂ evolution (μmol g ⁻¹ h ⁻¹)	Photoconductivity (φΣμ, 10 ⁻⁵ cm ² V ⁻¹ s ⁻¹)
AntCOF150	660	Amorphous	AB	Upto 540	2.40	55±5	1.2
BtAntCOF	588	Semicrystalline	AB	Upto 590	2.13	102±8	0.6
AntCOF150 + BtCOF150 (1:1)						450±10	
BtCOF150	554	Semicrystalline	AA	Upto 615	2.00	750±25	3.2
BtTpCOF	790	Semicrystalline	AA	Upto 590	2.12	450±10	1.0
BtCOF150 + TpCOF150 (1:1)						540±18	
TpCOF150	665	Semicrystalline	AA	Upto 540	2.36	50±4	1.1

References:

1. Rappe, A. K. et. al. UFF, a full periodic table force field for molecular dynamics simulations, *J. Am. Chem. Soc.* **114**, 10024-10035 (1992).
2. Lukose, B. et. al. The structure of layered covalent-organic frameworks, *Chem. Eur. J.* **17**, 2388-2389 (2011).
3. Aradi, B., Hourahine, B. & Frauenheim, T. DFTB+, a sparse matrix-based implementation of the DFTB method, *J. Phys. Chem. A* **111**, 5678 (2007).
4. Gaus, M., Goez, A. & Elstner, M. Parametrization and benchmark of DFTB3 for organic molecules, *J. Chem. Theory Comput.* **9**, 338 (2013).
5. Gaus, M., Lu, X., Elstner, M. & Cui, Q. Parametrization of DFTB3/3OB for sulphur and phosphorous for chemical and biological applications, *J. Chem. Theory Comput.* **10**, 1518 (2014).
6. Zhechkov, L. et. al. An efficient a posteriori treatment for dispersion interaction in density-functional-based tight binding, *J. Chem. Theory Comput.* **41**, 841 (2005).

7. Momma, K. & Izumi, F. VESTA 3 for three-dimensional visualization of crystal, volumetric and morphology data, *J. Appl. Crystallogr.* **44**, 1272 (2011).
8. Materials Studio, version 8.0, BIOVIA Software Inc., San Diego, CA, (2014).
9. Gaussian 09, Revision D.01, M. J. Frisch, G. W. Trucks, H. B. Schlegel, G. E. Scuseria, M. A. Robb, J. R. Cheeseman, G. Scalmani, V. Barone, B. Mennucci, G. A. Petersson, H. Nakatsuji, M. Caricato, X. Li, H. P. Hratchian, A. F. Izmaylov, J. Bloino, G. Zheng, J. L. Sonnenberg, M. Hada, M. Ehara, K. Toyota, R. Fukuda, J. Hasegawa, M. Ishida, T. Nakajima, Y. Honda, O. Kitao, H. Nakai, T. Vreven, J. A. Montgomery, Jr., J. E. Peralta, F. Ogliaro, M. Bearpark, J. J. Heyd, E. Brothers, K. N. Kudin, V. N. Staroverov, R. Kobayashi, J. Normand, K. Raghavachari, A. Rendell, J. C. Burant, S. S. Iyengar, J. Tomasi, M. Cossi, N. Rega, J. M. Millam, M. Klene, J. E. Knox, J. B. Cross, V. Bakken, C. Adamo, J. Jaramillo, R. Gomperts, R. E. Stratmann, O. Yazyev, A. J. Austin, R. Cammi, C. Pomelli, J. W. Ochterski, R. L. Martin, K. Morokuma, V. G. Zakrzewski, G. A. Voth, P. Salvador, J. J. Dannenberg, S. Dapprich, A. D. Daniels, Ö. Farkas, J. B. Foresman, J. V. Ortiz, J. Cioslowski, and D. J. Fox, Gaussian, Inc., Wallingford CT, 2009.
10. Ronson, T. K., Meng, W. & Nitschke, J. R. Design principles for the optimization of guest binding in aromatic-paneled $\text{Fe}^{\text{II}}_4\text{L}_6$ cages. *J. Am. Chem. Soc.* **139**, 9698–9707 (2017).